Article:

Li, B., Zhang, J. and Zhang, X. (2025) Optimal dispatch of an electricity-thermal-hydrogen microgrid for zero-carbon airport operations with electric and hydrogen aircraft. eTransportation. ISSN: 2590-1168

https://doi.org/10.1016/j.etran.2025.100485 eTransportation 27 (2026) 100485

Contents lists available at ScienceDirect

eTransportation

journal homepage: www.journals.elsevier.com/etransportation

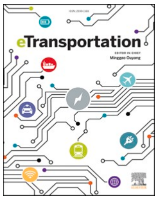

Optimal dispatch of an electricity-thermal-hydrogen microgrid for zero-carbon airport operations with electric and hydrogen aircraft

Bozheng Li [a], Jinning Zhang [b,*], Xin Zhang [a]

[a] School of Electrical and Electronic Engineering, University of Sheffield, Sheffield, United Kingdom
[b] School of Engineering, University of Leicester, Leicester, United Kingdom

ARTICLE INFO

Keywords:
Airport energy system
Multi-energy microgrid
Battery and hydrogen powered aircraft
Grid support flexibility

ABSTRACT

Achieving net-zero aviation requires airport energy infrastructure that delivers an efficient, reliable, and diversified energy supply to support the parallel operations of emerging battery-electric, hybrid hydrogen-electric, and hydrogen-powered aircraft. This study assesses how airport energy systems can support the transition to zero-carbon aviation. We propose an integrated electricity-thermal-hydrogen microgrid that incorporates photovoltaics, hydrogen fuel cells, and multiple energy storage systems to reduce reliance on the power grid and external energy sources. Firstly, a refined statistical method utilizing surrogate models is developed to estimate aircraft charging and refuelling demands. A stochastic optimization model that exploits load shifting potential is then formulated to minimize total economic costs while reducing operational risks and enhancing grid support flexibility. The resulting optimal energy dispatch ensures that flight schedules and multi-energy demands are met across electricity, thermal, and hydrogen networks. Case studies based on real flight schedules from Manchester airport evaluate five energy dispatch scenarios with varying optimization priorities. The results demonstrate a 29.4 % increase in grid flexibility and a 63.2 % reduction in operational risks through the proposed multi-energy dispatch strategy. Furthermore, sensitivity analyses examine the impacts of electricity and hydrogen price fluctuations, as well as different aircraft integration ratios, identifying the optimal electricity-to-hydrogen energy demand ratio for efficient airport energy system operation. These findings provide practical insights for airport operators and policymakers in developing resilient and sustainable airport energy infrastructure, and in implementing effective energy strategies for zero-carbon airport operations.

1. Introduction

1.1. Background and motivation

Civil aviation has expanded rapidly, driven by technological advances and global transport demands. However, this growth has resulted in substantial environmental challenges, as aviation remains one of the most energy-intensive transportation modes, with emissions increasing nearly sevenfold between 1960 and 2018 [1]. Sustainability has therefore become the aviation sector's central challenge, requiring transformative energy solutions [2].

Although recent technological advances have improved efficiency, aviation's expansion continues to outpace these gains through increasing air pollution. Achieving significant emissions reductions therefore requires an integrated energy strategy that incorporates alternative energy sources, operational optimization, and market-based measures [3]. The UK Aerospace Technology Institute (ATI) has highlighted the importance of developing aircraft technologies capable of utilizing novel energy sources, particularly hydrogen fuel and battery systems. This is crucial for achieving the UK's Net Zero target and realizing carbon-free airport operations by 2050 [4].

Aviation electrification represents a promising pathway toward airport decarbonisation when supported by renewable energy, however, its viability is constrained by the insufficient energy density of current battery technologies for aircraft propulsion. State-of-the-art lithium-ion batteries provide approximately 300 Wh/kg compared to 12,000 Wh/kg for jet fuel, highlighting a substantial performance gap [5,6]. Battery-powered aircraft also face considerable infrastructure challenges, particularly the need for megawatt-level ultra-fast charging facilities to meet short flight turnaround times, far beyond current electric vehicle (EV) charging capabilities [7,8]. Furthermore, batteries are vulnerable to thermal runaway, which requires advanced multi-layered

---

* Corresponding author.
E-mail address: jz388@leicester.ac.uk (J. Zhang).

https://doi.org/10.1016/j.etran.2025.100485
Received 17 April 2025; Received in revised form 25 August 2025; Accepted 15 September 2025

thermal management [9]. Consequently, the applications of battery technologies are largely limited to short-range operations, such as eVTOLs and regional flights, with significant barriers to adoption in larger commercial aircraft [7].

Green hydrogen offers superior gravimetric energy density than jet fuel, yet its lower volumetric energy density requires larger fuel storage and poses significant aircraft design challenges [10]. Large-scale adoption of hydrogen propulsion also requires extensive renewable capacity for green hydrogen production via electrolysis and substantial capital investment in distribution infrastructure, whether through gaseous pipelines or liquid hydrogen transportation systems [11]. Moreover, hydrogen propulsion introduces safety concerns such as flammability and explosion risks, also requiring advanced safety measures, including leak detection, ventilation control, and impact-resistant storage [12]. Despite these challenges, hydrogen is widely recognized as a viable medium-to-long-term solution for zero-carbon aviation. For example, the ATI's FlyZero project has identified liquid green hydrogen as the most promising option, capable of supporting over 90 % of long-haul flights [13].

Hybrid hydrogen-electric propulsion architectures offer a synergistic approach that leverages the complementary advantages of both battery and hydrogen technologies. Such a hybrid powertrain offers redundancy to enhance operational safety and enables continued operation after single-point failures [14]. More broadly, certification frameworks for electric and hydrogen propulsion have entered an early and research-intensive stage, with published roadmaps and established working groups dedicated to identifying safety hazards, assessing regulatory gaps, and guiding the development of future standards [15–17].

In light of current technological limitations, zero-carbon aviation is expected to require a dual-pathway approach: battery-powered aircraft for short-haul and regional flights, while hybrid hydrogen-electric and hydrogen propulsion for medium- and long-haul commercial operations. This transition will fundamentally reshape airport energy management strategies, necessitating substantial upgrades to the supporting airport energy infrastructure.

1.2. *Literature review*

As future airports are expected to face surging electricity and hydrogen demands, accurately quantifying energy requirements will be essential for designing low-carbon integrated energy systems and management strategies. Recent studies have begun to address airport energy demand modelling and analysis, focusing primarily on electrified ground support equipment (GSE) and EVs. Ref. [18] compared energy consumption across electric, hybrid, and zero tow-tractor scenarios using Mixed Integer Linear Programming (MILP) optimization, demonstrating that hybrid towing can effectively reduce energy use under stochastic conditions and varying traffic density. Ref. [19] developed a more detailed fuel consumption model for aircraft taxiing, incorporating aircraft engine characteristics and thrust levels to evaluate e-tractor utilization. For EV operations in airports, simulation-based optimization model and fuzzy logic approaches have been applied to identify optimal battery capacity, charging power, and infrastructure requirements for airport shuttle buses [20,21]. Ref. [22] presented a multi-agent simulation model for all-electric airport shuttle transportation networks, estimating average power demands of 10 MW with peak demands reaching around 12 MW at a regional UK airport. However, such modelling and simulation methods are unsuitable for quantifying aircraft energy demands, given the fundamentally different operational patterns and energy requirements of aircraft compared to ground vehicles.

Several studies have examined the potential energy demands of electrified aircraft. Existing research has classified domestic flights to estimate hybrid electric aircraft energy requirements, analysed simplified charging scenarios for small electric aircraft, and applied detailed energy consumption models for medium-sized all-electric aircraft based on existing commercial design models [23–26]. Although research advances have improved mission and payload specific modelling, most existing analyses focus on single aircraft types without comparative evaluation. Preliminary assessments of plug-in charging versus battery-swapping approaches have been conducted, exploring grid flexibility potential but constrained by fixed charging powers and partial electrification scenarios [27]. However, comprehensive evaluations of energy demands for hybrid hydrogen-electric and purely hydrogen-powered aircraft have yet to be thoroughly investigated.

Research on airport energy supply has increasingly emphasizes distributed energy resources, including both single-source and integrated multi-energy systems. Recent studies on single-source applications have demonstrated significant potential for airport-based photovoltaic (PV) systems across various scales and geographic locations. Assessment of 5–20 MW PV installations at airports in India, UK, and Malaysia using RETScreen, SISIFO/GSA, SolarGis models, respectively, have shown satisfactory performance and feasibility while maintaining safe airport operations [28–30]. Notably, the UK study further highlighted seasonal energy transfer, storing or shifting surplus summer generation for winter use, can enhance grid flexibility through load balancing and peak shaving. On a larger scale, analysis of over 200 Chinese airports [31] identified a combined PV capacity of 2.50 GW, nearly matching annual electricity demands in eight provinces, highlighting the immense potential of airports to contribute to regional energy supply through on-site PV generation systems.

For integrated multi-energy systems, research has explored renewable energy integration and management frameworks at airports, encompassing both conventional renewables, emerging hydrogen technologies, and advanced optimization strategies. Several studies have developed integrated multi-energy systems combining wind turbines, PV, waste-to-energy, geothermal, and biomass resources, validated through predictive control and dynamic thermodynamic simulations [32,33]. Others have focused on hydrogen integration, exploring hydrogen-powered aviation scenarios, airports as regional hydrogen hubs, and system resilience through lifecycle-based optimization [34–36]. Furthermore, Ref. [37] advanced this work by establishing a multi-energy airport microgrid integrating hydrogen supply, electric auxiliary power units (APUs), EVs, PV, and both battery and hydrogen storage. MILP-based optimization with various energy scenarios demonstrated substantial techno-economic benefits. However, comprehensive studies that incorporate large-scale adoption of electric and hydrogen aircraft demands, as well as the coupling of thermal, electric, and hydrogen energy networks, remain limited.

Beyond optimizing airport onsite energy supply, recent research has explored interactions between airport electrification facilities and external power grids or hydrogen networks, considering their bidirectional flexibility as generation, demands and energy storage. Ref. [21] noted that airport surplus PV and WT generation during periods of high solar irradiance and wind availability could be sold to the grid, reducing operational costs while enhancing sustainability. Ref. [38] assessed EV battery flexibility for peak shaving and valley filling, while Ref. [39] extended this research to explore interactive capabilities of both EVs and electric aircraft batteries, achieving multi-objective optimized scheduling that enhances self-consumption. Ref. [22] investigated bidirectional wireless charging for electric buses, highlighting its potential to mitigate grid stress and enhance resilience in high-density, high-load airport scenarios. Airport electrified facilities can also provide ancillary grid services. Ref. [40] demonstrated the profitability of electrified GSE participating in frequency regulation markets through V2G technology. Ref. [41] introduced the aviation-to-grid (A2G) concept, it shows that electric aircraft charging could deliver more than 1 GW of frequency response across eight UK airports, enhancing both grid stability and economic viability. However, research work on hydrogen networks remains limited, primarily focusing on small-scale procurement due to the lack of established pricing mechanisms and market structures [42,43]. Overall, comprehensive investigations into airport multi-energy

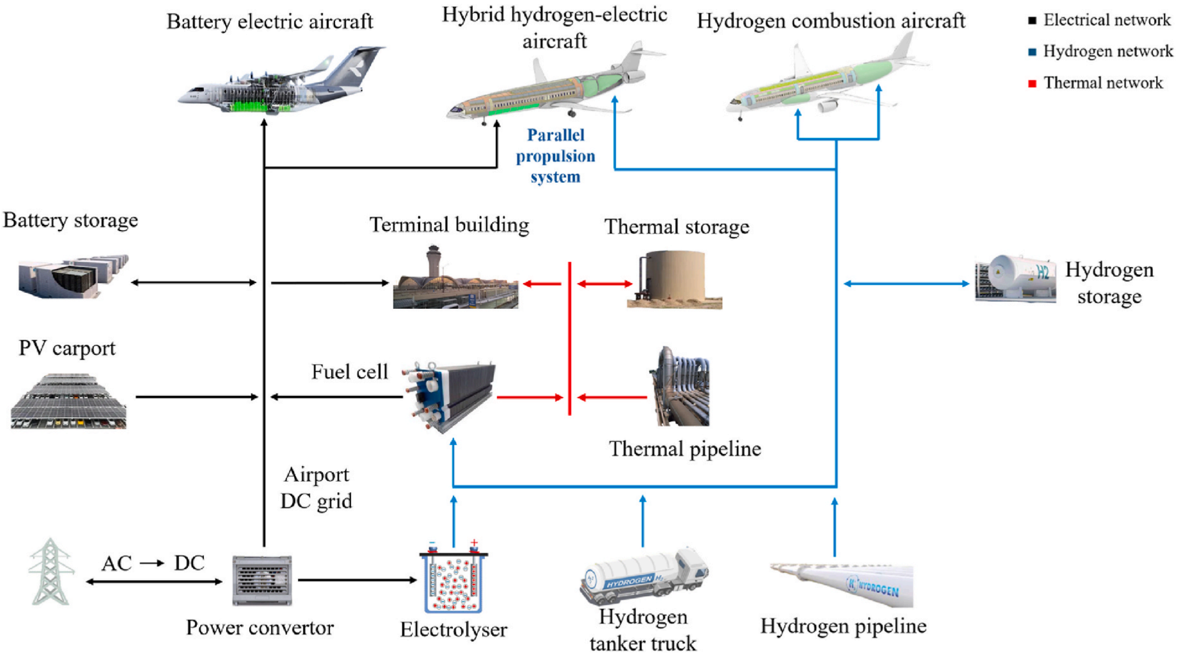

Fig. 1. Integrated electricity-thermal-hydrogen airport microgrid structure.

microgrids, their energy interaction and conversion with grid support services, are underdeveloped.

In summary, existing literature largely focuses on terminal, electric GSE, and aircraft APU energy supplies via distributed microgrids but neglects zero-carbon aviation energy needs for electric and hydrogen aircraft, leaving significant research gaps. Additionally, current studies give limited attention to the flexibility of electric or hydrogen aircraft. They also overlook the holistic optimization of aviation operations and airport energy systems. Such an integrated approach is needed to fully leverage their potential in supporting net-zero aviation.

1.3. Contributions and structure

In this paper, an integrated electricity-thermal-hydrogen energy system is proposed to assess the feasibility of operating an airport microgrid under significant hydrogen and electricity demands from hydrogen- and battery-powered aircraft. To evaluate airport system performance, a comprehensive energy dispatch optimization model is developed that accounts for the stochastic nature of PV generation and actual flight schedules. Finally, a sensitivity analysis of energy prices and aircraft integration ratios is thoroughly examined to guide future zero-carbon airport energy infrastructure operations.

There are three main contributions outlined as follows:

- To the best of our knowledge, this study introduces the first refined statistical method utilizing a surrogate model to estimate charging and refuelling demands for all-electric, hybrid hydrogen-electric, and hydrogen-powered aircraft. By capturing differentiated power consumption characteristics across aircraft models, energy patterns and flight phases, this method enables detailed analysis of zero-carbon airport energy requirements and establishes a foundation for feasibility assessment of future airport energy systems.
- A comprehensive energy dispatch optimization model is proposed for multi-energy airport microgrids, aiming to minimize total economic costs while reducing operational risks and improving flexibility, subject to flight schedules and aircraft energy demands under the stochastic nature of renewable energy generation.
- A detailed sensitivity analysis is performed on electricity and hydrogen prices and aircraft integration ratios, offering insights into the operational performance and adaptability of the airport energy systems in support of net-zero aviation.

The paper is organised as follows: Section 2 describes the structure of the proposed airport energy system. Section 3 presents the optimization framework for airport microgrid energy dispatch. The optimization methodology is illustrated in Section 4. Results and discussion are provided in Section 5, and conclusions are drawn in Section 6.

2. Airport microgrid energy supply and demand analysis

2.1. Airport microgrid structure and energy supply-demand network

Achieving zero-carbon airport energy systems requires the adoption of clean energy aircraft. This paper considers a feasible technical pathway from conventional fleets to all-electric, hydrogen-powered, and hybrid hydrogen-electric aircraft, as illustrated in Fig. 1. The hybrid hydrogen-electric aircraft use batteries and hydrogen fuel cells (HFCs), thereby achieving higher energy conversion efficiency and enabling longer flight ranges. Hydrogen aircraft rely on combustion for the thrust required by larger and long-haul aircraft. This transition introduces substantial electricity and hydrogen demands, fundamentally reshaping airport energy systems and distinguishing airport microgrids from conventional ones.

Airport demand profiles typically demonstrate significantly lower load factors compared to industrial or residential systems. This is largely due to the pronounced peak-to-average ratios driven by aircraft arrival and departure patterns, resulting in substantial temporal load variability that requires flexible and responsive energy management strategies.

Airport energy systems also integrate multiple energy vectors, including not only the electric and hydrogen demands from aircraft but also the electricity and heating loads of terminal buildings, thus requiring coordinated energy optimization across electricity, hydrogen, and thermal networks. Furthermore, airport microgrids are subject to rigid temporal constraints imposed by flight schedules. Critical operations such as electric aircraft charging and hydrogen refuelling must be completed within predefined turnaround windows, resulting in less flexible, time-bound demand profiles. These operations often involve megawatt-scale instantaneous electric and hydrogen demands, requiring infrastructure capable of handling intense short-term loads, unlike the more gradual and predictable load profiles observed in conventional microgrids. To address these unique challenges, this paper proposes a novel integrated multi-energy microgrid structure for airports as illustrated in Fig. 1. This airport microgrid incorporates electricity-thermal-hydrogen energy networks with large-scale renewable power generation, multi-energy conversion technologies, and diverse storage capabilities.

Specifically, the airport microgrid comprises PV arrays as the primary renewable energy source, alongside dispatchable energy conversion equipment including HFC and electrolysers. Energy storage devices consist of battery energy storage systems (BESS), hydrogen storage tanks (HST), and thermal storage tanks (TST). In addition to aircraft electricity and hydrogen demands, the microgrid also needs to satisfy the thermal loads of airport terminal buildings, which is typically used for space heating and hot water preparation [44]. The primary objective of day-ahead optimization is to meet the airport's flight schedules and operational constraints while maximizing overall system performance. The multi-energy dispatch is optimized at 20-min intervals to achieve the optimal dispatch plan for the next 24 h. As a renewable power source, PV generation is inherently variable and non-dispatchable due to its direct dependence on weather conditions. Hydrogen produced through water electrolysis serves as a supplement to externally purchased hydrogen when economically beneficial. The HFC units utilize hydrogen to simultaneously generate electricity and recoverable heat, with an adjustable thermoelectric output ratio. Recovered waste heat from these processes is collected through a heat recovery system to supplement external heat purchases in meeting the thermal loads of terminal buildings.

2.2. Aircraft electric and hydrogen demand modelling

Previous research on estimating aircraft energy demands for integrated airport energy systems has typically relied on simplified and single-source demand profiles derived directly from flight schedule data. For example, several studies utilized average or constant electric aircraft charging assumptions, assigned fixed charging durations within turnaround intervals [37,45,46], or evenly divided conventional aircraft missions into multiple electric missions [27]. These simplifications generally assume a linear relationship between aircraft energy consumption and flight distance, neglecting significant variations in aircraft types, sizes, and operational phases. Such assumptions fail to adequately capture the true complexity of real-world airport operations, where diverse fleets with heterogeneous energy consumption characteristics coexist. Consequently, relying on simplified aircraft energy demand profiles can compromise the accuracy and effectiveness of energy management strategies, highlighting the necessity for more sophisticated aircraft demand modelling methods. In addition, hybrid hydrogen-electric aircraft create multi-source demand profiles beyond electricity, while hydrogen also plays an important role in aircraft demand modelling, introducing new coupling points between electricity and hydrogen in aircraft propulsion technologies.

To overcome these limitations and enhance the precision of aircraft demand modelling, this study adopts a detailed aircraft point-mass model coupled with surrogate modelling techniques, as shown in Fig. 2. Specifically, typical flight missions are input into a high-fidelity aircraft dynamic model to simulate flight trajectories and energy demands across critical operational phases from takeoff to landing. The simulation outputs then serve as training datasets to establish surrogate models. After deriving aircraft energy demands through the surrogate models, electric charging or hydrogen refuelling power requirements are subsequently determined based on predefined charging and refuelling durations. With charging power and duration established, aircraft demand shifting essentially involves adjusting the timing of charging or refuelling within the allowable turnaround windows at the airport. This scheduling adjustment is conducted to align with the optimization objectives of the airport microgrid, ensuring that operational constraints are satisfied while maximizing energy dispatch efficiency.

2.2.1. High-fidelity evaluation of aircraft energy consumption

To accurately determine the energy demand of aircraft for surrogate model training, representative flight distances corresponding to typical operational missions of all aircraft types are initially sampled. These sampled data points are subsequently input into a point-mass aircraft model to precisely simulate aircraft dynamic trajectories and energy consumption. Specifically, the adopted point-mass model accurately describes aircraft motion through the following system of equations [47]:

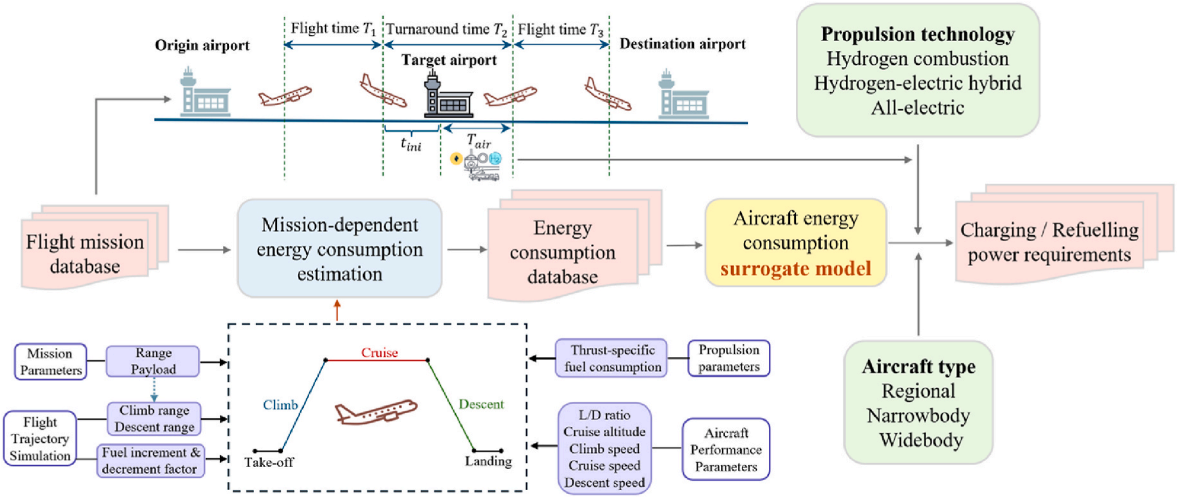

Fig. 2. Flowchart of aircraft energy demand modelling.

$$\begin{bmatrix} \frac{dx}{dt} \\ \frac{dy}{dt} \\ \frac{dh}{dt} \\ \frac{dV}{dt} \\ \frac{d\psi}{dt} \\ \frac{d\gamma}{dt} \end{bmatrix} = \begin{bmatrix} v\cos(\psi)\cos(\gamma) \\ v\sin(\psi)\cos(\gamma) \\ v\sin(\gamma) \\ \frac{1}{m}[F\cos(\alpha) - R - mg\sin(\gamma)] \\ \frac{1}{mv\cos(\gamma)}[F\sin(\alpha) + S]\sin(\mu) \\ \frac{1}{mv}[(F\sin(\alpha) + S)\cos(\mu) - mg\cos(\gamma)] \end{bmatrix} \tag{1}$$

where x, y, h represent aircraft positions in the ground-axis coordinate system, v denotes the aircraft velocity relative to the ground, μ, γ, ψ are roll bank, flight path, and yaw heading angle respectively, and m indicates the mass of aircraft. Additionally, R, S, F represent the forces of lift, drag, and thrust acting on the aircraft, g denotes the gravitational acceleration and α indicates the angle of attack. Parameters for each flight and its corresponding aircraft propulsion and performance characteristics are sourced from open-access databases.

From Eq. (1), the equilibrium of forces acting on the aircraft at any moment is formulated in Eq. (2) and illustrated in Fig. 3:

$$m\frac{d\vec{v}}{dt} = \vec{F} + \vec{S} + \vec{R} + \vec{W} \tag{2}$$

By adopting the velocity magnitude v and flight path angle γ as coordinate variables, and projecting the forces onto both tangential and normal directions of the wind-axis system, two scalar equations describing longitudinal motion are derived [48].

$$\begin{cases} m\frac{\mathrm{d}}{\mathrm{d}t}v + mg\sin\gamma = T\cos\alpha - \frac{1}{2}C_D\rho Sv^2 \\ mv\frac{\mathrm{d}}{\mathrm{d}t}\gamma + mg\cos\gamma = T\sin\alpha + \frac{1}{2}C_L\rho Sv^2 \end{cases} \tag{3}$$

where S denotes the wing area, ρ is air density, $C_D(\alpha)$ and $C_L(\alpha)$ are drag and lift coefficients respectively, each dependent on angle of attack α. Accordingly, the propulsion drive power at any instant can be obtained as:

$$P_{drv} = \vec{T}\cdot\vec{v} = m\frac{d}{dt}\left(\frac{1}{2}v^2\right) + \frac{1}{2}C_D\rho Sv^3 + mgv\sin\gamma \tag{4}$$

For hybrid hydrogen-electric aircraft configured with parallel propulsion architectures, assuming 100 % drivetrain efficiency, the total propulsion power at time t is expressed as:

$$P_{drv}(t) = P_{H_2}(t) + P_{ele}(t) \tag{5}$$

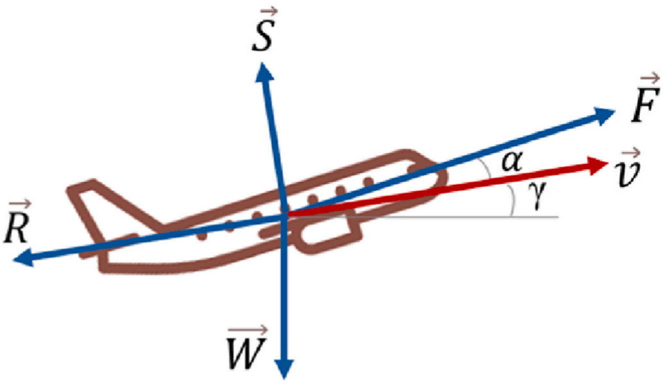

Fig. 3. Aircraft equilibrium forces in aircraft motion.

Thus, the overall energy consumption required for each complete flight mission is calculated by integrating the propulsion power throughout the flight trajectory:

$$E_{trip} = \int P_{drv}(t)dt = \int P_{H_2}(t)dt + \int P_{ele}(t)dt \tag{6}$$

The precise aircraft energy consumption data derived from this rigorous point-mass simulation approach subsequently serve as training datasets for constructing surrogate models.

Surrogate models refer to mathematical approximations designed to replace computationally expensive simulations while preserving satisfactory accuracy. Surrogate modelling generally involves two key phases: training and prediction [49]. During prediction, given input parameters a and model parameters k, surrogate models predict output variables b:

$$b = f(a, k) \tag{7}$$

During training, surrogate model parameters k are optimized to minimize discrepancies between surrogate predictions and actual observations across the training dataset [50]:

$$b_i \approx f(a_i, k), \forall 1 \le i \le m \tag{8}$$

Among various surrogate modelling approaches, Universal Kriging, a robust interpolation method capable of accommodating global data trends, is selected in this study. It can accurately model aircraft energy consumption patterns exhibiting systematic variation across different operational phases (take-off, climb, cruise, descent, and landing), thus providing superior predictive fidelity over conventional linear regression models. In Universal Kriging method, the prediction at a given point is calculated through polynomial trend and correlation components, represented mathematically as [51]:

$$f(x, w) = \sum_{i=1}^{n_p} p_i(x)a_i + \sum_{i=1}^{n_t} \psi_i(x)b_i \tag{9}$$

This is concisely expressed in matrix form as:

$$y = Pa + \Psi b \tag{10}$$

The surrogate models developed using this integrated approach can precisely represent aircraft energy demands across typical operational scenarios. This enhanced accuracy and computational efficiency will enable effective energy dispatch optimization and operational planning for future airport microgrids incorporating electric and hydrogen aircraft.

2.2.2. Aircraft charging and refuelling strategy exploiting demand shifting potential

Once surrogate models accurately predict aircraft energy consumption, it is essential to determine the corresponding electric charging or hydrogen refuelling durations to obtain the final power demands. In this study, constant charging and refuelling power assumptions are adopted, facilitating the implementation of demand shifting strategies. Specifically, based on passenger capacity and flight range, the existing aircraft fleet is classified and mapped into three categories of zero-emission aircraft, each with tailored charging or refuelling durations T_{air}, as summarised in Table A1. All regional aircraft are replaced by all-electric aircraft with a fixed charging duration of 40 min, while single-aisle narrow-body aircraft, such as the Boeing 737, are substituted with hybrid electric-hydrogen aircraft that retain the same charging/refuelling duration. Twin-aisle wide-body aircraft with approximately 300 seats are uniformly replaced by hydrogen combustion aircraft, considering current battery technology limitations and their typically longer flight mission profiles. Accordingly, their refuelling duration is set to 1 h. In contrast, ultra-large double-deck aircraft, such as the Boeing 747 and Airbus A380, are excluded from the scope of zero-emission aircraft modelling due to their limited operational frequency at most UK airports and greater viability for sustainable aviation fuel (SAF)-based operations [4].

Moreover, in practical airport operations, additional reserve fuel beyond the necessary trip energy is also typically provided for flight safety and operational contingencies [52]. Therefore, as indicated in Table A1, this study includes reserve energy margins of 10 % for electric and hybrid aircraft, and 15 % for hydrogen aircraft, calculated based on the predicted trip energy from the surrogate models. Furthermore, besides the flight duration from the target airport to the destination T_3, other critical parameters such as the flight duration from the origin airport to the target airport T_1 and the turnaround time T_2 are also considered, as shown in Fig. 2. By inputting T_1 into the developed surrogate model, the energy consumption from the preceding flight segment can be accurately determined, and the corresponding reserve energy will then serve as the initial energy state of the aircraft upon arrival at the airport, rather than assuming a zero initial state.

Consequently, the final charging or refuelling power demand for each aircraft i at the target airport can be mathematically formulated as follows:

$$P_i^{\mathrm{req}} = \frac{E_i^{\mathrm{req}}}{T_{\mathrm{air}}^i} = \frac{(1+\lambda_{res})\cdot E_{trip}(T_3) - E_{res}(T_1)}{T_{\mathrm{air}}^i} \tag{11}$$

where $E_{trip}(T_3)$ is the predicted trip energy obtained through the surrogate model for the subsequent flight departing from the target airport, $E_{res}(T_1)$ is the reserve energy determined by the energy consumption of the incoming flight, λ_{res} represents the reserve energy ratio, and T_{air}^i denotes the predefined constant charging or refuelling duration.

To further realize demand shifting capabilities, it is necessary to determine the turnaround time of each aircraft T_2 and subsequently adjust the timing of charging or refuelling within this available window. Specifically, the flight schedule dataset used in this study includes comprehensive arrival and departure information, encompassing flight numbers and times, aircraft tail numbers, and origin/destination airports [53]. Aircraft tail numbers serve as unique identifiers, enabling accurate tracking and pairing of arrival and departure records. For instance, as shown in Table A2 and Table A3, aircraft tail number B-LRT (Airbus A350-900) arrived at the airport at 07:55 (flight CX219) and departed at 10:25 (flight CX216), yielding a turnaround time of 2.5 h. This turnaround interval defines the available window during which charging or refuelling power demands can be flexibly shifted and scheduled according to airport energy system optimization requirements.

Specifically, a normalized variable $\lambda_{i,t}$ is introduced to represent the proportion of the total required charging or refuelling energy E_i^{req} allocated to time step t, for aircraft i. The charging/refuelling load at each time step t is then formulated as:

$$L_t^{Airport} = \sum_{i\in\mathscr{A}_t} \frac{E_i^{\mathrm{req}}}{\Delta t}\cdot\lambda_{i,t} \tag{12}$$

subject to the constraints:

$$\sum_{t=t_i^{arr}}^{t_i^{dep}} \lambda_{i,t} = 1, \lambda_{i,t} = 0 \quad \forall t \notin \left[t_i^{arr}, t_i^{dep}\right] \tag{13}$$

where $L_t^{Airport}$ is the total aircraft charging/refuelling load at time step t, Δt denotes the duration of each time step, t_i^{arr}, t_i^{dep} are the arrival and departure times of aircraft i, $\mathscr{A}_t$ represents the set of aircraft present at the airport at time t. The charging/refuelling demand of each aircraft is fully met within turnaround time through demand shifting windows, which demonstrate temporal flexibility for energy demand scheduling within operational constraints.

In summary, the presented methodology integrates detailed point-mass aircraft modelling with surrogate model techniques to accurately predict aircraft energy consumption. Constant-power charging/refuelling assumptions and reserve energy considerations are then applied to transform obtained electric and hydrogen energy demands into power requirements. By leveraging precise turnaround time identification based on the actual flight schedule data, the proposed approach effectively enables flexible demand shifting, enhancing operational flexibility and efficiency for the energy management of future airport microgrids.

3. Problem formulation

3.1. Multi-energy microgrid model

3.1.1. Electrical energy network modelling

(1) Airport PV system

At airports, PV systems can be installed not only on suitable ground areas around the airport but also on the rooftops of airport buildings, including terminals and car parks, thereby maximizing the use of available space and minimizing the land footprint required for renewable energy generation [41].

The PV output power exhibits a strong dependence on solar irradiance intensity and ambient temperature conditions. Based on statistical analysis, the solar irradiance intensity over a given time interval can be effectively approximated using a Beta distribution. The corresponding probability density function is formulated as [54]:

$$\left(\frac{G}{G_{max}}\right) = \frac{\Gamma(\alpha+\beta)}{\Gamma(\alpha)\Gamma(\beta)}\left(\frac{G}{G_{max}}\right)^{\alpha-1}\left(1-\frac{G}{G_{max}}\right)^{\beta-1} \tag{14}$$

where Γ represents the Gamma function; G and G_{max} denote the actual and maximum solar irradiance intensity during the given period, respectively; α and β are shape parameters of the Beta distribution, which are derived from the standard deviation σ and mean value μ of the solar irradiance intensity during this time period.

The PV output power can be estimated by comparing the solar irradiance intensity at standardized testing parameters with the actual operating conditions, in considering ambient temperature [54], as expressed in Eq. (15):

$$P_{\mathrm{PV}}(G, T_{pv}) = P_{\mathrm{STP}}\frac{G}{G_{\mathrm{STP}}}\left[1 + k\left(T_{pv} - T_{\mathrm{STP}}\right)\right] \tag{15}$$

where STP represent PV operation at standardized test condition; G_{STP} denotes the solar irradiance intensity under STP, set at 1000 W/m^2; T_{STP} represents the standard reference temperature, defined as 25 °C; G is the actual solar irradiance intensity; k represents the power temperature coefficient; and T_{pv} denotes the surface operating temperature of the PV array.

(2) Battery energy storage system

The BESS is a critical component in the integrated energy system, performing multiple essential functions, such as alleviating renewable energy volatility, improving power quality, and facilitating peak shaving and valley filling [55]. In this airport microgrid, Li-ion batteries are selected for the BESS on account of their superior technical features, including rapid charging capabilities, minimal self-discharge rates, high energy density, and excellent safety features.

Unlike conventional models that assume constant efficiency values, this study incorporates part-load efficiency characteristics to accurately capture the BESS performance under varying operating conditions. The state of charge (SoC) of the BESS at a given time t can be described as:

$$SOC_{\mathrm{BESS}}(t) = SOC_{\mathrm{BESS}}(t-1)\cdot(1-\sigma_{\mathrm{BESS}}) + \left(\eta_{\mathrm{BESS}}^{\mathrm{ch}}\cdot P_{\mathrm{BESS}}^{\mathrm{ch}}(t) - \frac{P_{\mathrm{BESS}}^{\mathrm{dis}}(t)}{\eta_{\mathrm{BESS}}^{\mathrm{dis}}}\right)\cdot\frac{\Delta t}{E_{\mathrm{BESS}}^{\mathrm{max}}} \tag{16}$$

where $SOC_{\mathrm{BESS}}(t)$ denotes the charging state of the BESS at time t, $P_{\mathrm{BESS}}^{\mathrm{ch}}(t)$ and $P_{\mathrm{BESS}}^{\mathrm{dis}}(t)$ are the power charged to and discharged from the BESS at time t, respectively. The coefficient σ_{BESS} is the self-discharge rate, which is treated as a constant value in this study, as its variation becomes significant only in long-duration simulations on the scale of weeks or months, consistent with common practice in short-term dispatch studies [56]. Notably, $\eta_{\mathrm{BESS}}^{\mathrm{ch}}$ and $\eta_{\mathrm{BESS}}^{\mathrm{dis}}$ are power-dependent efficiency functions rather than constant values, reflecting the part-load characteristics of the BESS. $E_{\mathrm{BESS}}^{\max}$ represents the maximum capacity of the BESS.

Battery degradation represents a significant economic consideration in BESS operation. Based on the cumulative damage model developed by the U.S. National Renewable Energy Laboratory (NREL), each discharge cycle contributes to irreversible battery degradation [54]. The total useable energy throughput before end-of-life is expressed as:

$$E_{life} = L_R \cdot D_R \cdot C_R \tag{17}$$

where C_R represents the rated capacity at the rated discharge current, D_R represents the rated depth of discharge (DoD) used to define the rated cycle life, and L_R represents the rated cycle life under standard operating conditions.

The effective throughput per discharge cycle is influenced by both the DoD and discharge rate. The relationship between DoD and cycle life follows:

$$L(D_A) = L_R \cdot \left(\frac{D_A}{D_R}\right)^{-u_0} \cdot \exp\left(-u_1 \cdot \left(\frac{D_A}{D_R} - 1\right)\right) \tag{18}$$

where $L(D_A)$ is the actual cycle life, D_A is actual depth of discharge, and u_0, u_1 are empirical fitting parameters.

The discharge rate effect on battery capacity is captured through:

$$C_A = C_R \cdot k_0 - I_A \tag{19}$$

where C_A is the actual discharge capacity, k_0 denotes an empirical coefficient, and I_A is the discharge current calculated from the battery cell power as:

$$I_A = P_{BESS}^{dis}(t) \cdot 10^6 \,/\, \left(\eta_{BESS}^{dis} \cdot U_{ESS}\right) \tag{20}$$

where U_{ESS} represents the battery system voltage.

Combining both effects of discharge depth and rate, the effective ampere-hour consumption per discharge cycle is defined as:

$$\begin{aligned} & d_{eff}(t) = k_{DOD}(t) \cdot k_{rate}(t) \cdot d_{act}(t) \\ & \text{where} \begin{cases} k_{DOD}(t) = \left(\dfrac{D_A(t)}{D_R}\right)^{u_0} \cdot \exp\left(u_1 \cdot \left(\dfrac{D_A(t)}{D_R} - 1\right)\right) \\ k_{rate}(t) = \dfrac{C_R}{C_A(t)} \\ d_{act}(t) = I_A(t) \cdot \Delta t \end{cases} \end{aligned} \tag{21}$$

where $d_{eff}(t)$ is the effective ampere-hour consumption at time t. $k_{DOD}(t)$ is the DoD impact factor. $k_{rate}(t)$ represents the discharge rate impact factor, $d_{act}(t)$ is the actual discharge in ampere-hours.

And the depth of discharge at time t is:

$$D_A(t) = 1 - SOC_{BESS}(t) \tag{22}$$

After obtaining the effective ampere-hour consumption per discharge cycle, the remaining battery life can be expressed as:

$$Y_{life}(t) = \frac{E_{life}}{\sum\limits_{i=1}^{t} d_{eff}(i)} \tag{23}$$

where $\sum_{i=1}^{t} d_{eff}(i)$ represents the accumulated effective ampere-hour consumption up to time t.

The comprehensive consideration of both DoD and discharge rate effects, along with part-load efficiency characteristics, ensures accurate assessment of the complex degradation mechanisms and operational economics inherent in BESS.

(3) Electrolysers

Currently, two types of electrolyser technologies are widely used for hydrogen production: alkaline electrolysers and proton exchange membrane (PEM) electrolysers. Among these technologies, PEM electrolysers offer several advantages including rapid response capabilities, wide operating range and high current density. Furthermore, PEM electrolysers demonstrate excellent dynamic performance with fast startup time and the ability to operate efficiently under partial load conditions, making them particularly suitable for coupling with intermittent renewable energy sources and responding to fluctuating hydrogen demand in airport microgrid systems [57]. Therefore, this study adopts PEM electrolysis as the hydrogen production method in the proposed airport microgrid model. The electrolyser model captures realistic operational characteristics by incorporating multiple operating states and part-load characteristics, reflecting the actual technical constraints and efficiency variations of commercial electrolysers. It should be noted that pressure ramping dynamics are not considered in this model, as the optimization time intervals (20 min) exceed typical pressure ramping periods of PEM electrolysers, and the hydrogen storage system is assumed to maintain constant pressure through dedicated regulation equipment [58].

The electrolyser operates in four distinct states: production, standby, startup, and shutdown. During production state, the hydrogen generation rate exhibits a non-linear relationship with power consumption due to varying efficiency across different operating loads:

$$m_{H_2}^t = f\left(P_{el,prod}^t, \eta_{el}\left(P_{el,prod}^t\right)\right) \quad \forall t \in T \tag{24}$$

where $m_{H_2}^t$ is the amount of hydrogen generated at time t; η_{el} represents the load-dependent efficiency and the electrical power input to the electrolyse is denoted as $P_{el,prod}^t$.

The total power consumption of PEM electrolysers comprises three components:

$$P_{el}^t = P_{el,prod}^t + P_{el,startup}^t + P_{el,standby} \cdot u_{standby}^t \quad \forall t \in T \tag{25}$$

where $P_{el,startup}^t$ denotes startup power consumption, $P_{el,standby}$ is the constant standby power requirement, and $u_{standby}^t$ is the binary standby state indicator.

3.1.2. Hydrogen energy network modelling

(1) Hydrogen storage tank

The HST serves as a reservoir for hydrogen produced through water electrolysis, providing hydrogen supply for both hydrogen-powered aircraft and hydrogen fuel cells. The hydrogen level in the HST at time t can be described as [59]:

$$SOC_{\mathrm{HST}}(t) = SOC_{\mathrm{HST}}(t-1) + \left(P_{\mathrm{HST}}^{\mathrm{ch}}(t) \cdot \eta_{\mathrm{HST}}^{\mathrm{ch}} - \frac{P_{\mathrm{HST}}^{\mathrm{dis}}(t)}{\eta_{\mathrm{HST}}^{\mathrm{dis}}}\right) \cdot \frac{\Delta t}{E_{\mathrm{HST}}^{\max}} \tag{26}$$

where $SOC_{\mathrm{HST}}(t)$ represents the state of charge of the HST at time t, $P_{\mathrm{HST}}^{\mathrm{ch}}(t)$ and $P_{\mathrm{HST}}^{\mathrm{dis}}(t)$ are the hydrogen charging and discharging rates at time t. The self-discharge factor $\sigma_{\mathrm{HST}} = 0$, as self-discharge effects are typically negligible for hydrogen storage. $\eta_{\mathrm{HST}}^{\mathrm{ch}}$ and $\eta_{\mathrm{HST}}^{\mathrm{dis}}$ represent the HST charging and discharging efficiency factors, while $E_{\mathrm{HST}}^{\max}$ represents the maximum capacity of the HST.

(2) Hydrogen fuel cell

Hydrogen fuel cells can reverse the energy conversion process of electrolysers, transforming stored hydrogen into electrical energy. The HFC model captures power and thermal outputs in relation to energy conversion efficiency and hydrogen consumption under varying load conditions.

The electrical power output of the fuel cell system is expressed as [59]:

$$P_{fc}^{t} = \eta_{fc,ele}^{t} \cdot \dot{m}_{fc,H_2}^{t} \cdot LHV_{H_2} \Big/ \Delta t \tag{27}$$

where P_{fc}^{t} is the electrical power output of fuel cell at time t, $\eta_{fc,ele}^{t}$ represents the electrical efficiency, $\dot{m}_{fc,H_2}^{t}$ denotes the hydrogen consumption rate (kg/ Δt), LHV_{H_2} is the lower heating value of hydrogen, and Δt is the time interval.

The thermal power generation from the fuel cell is characterized by:

$$Q_{fc}^{t} = \dot{m}_{fc,H_2}^{t} \cdot LHV_{H_2} \cdot \frac{\eta_{fc,th}^{t}}{\Delta t} \tag{28}$$

where Q_{fc}^{t} represents the thermal power output and $\eta_{fc,th}^{t}$ denotes the thermal efficiency of the fuel cell system.

3.1.3. Thermal energy network modelling

The TST serves dual functions in the airport microgrid: absorbing excess waste heat recovered from HFC operations, while providing thermal energy during periods of high heating load for the terminal building. The thermal energy level in the TST at time t can be expressed as [54]:

$$SOC_{\mathrm{TST}}(t) = SOC_{\mathrm{TST}}(t-1) + \left(P_{\mathrm{TST}}^{\mathrm{ch}}(t) \cdot \eta_{\mathrm{TST}}^{\mathrm{ch}} - \frac{P_{\mathrm{TST}}^{\mathrm{dis}}(t)}{\eta_{\mathrm{TST}}^{\mathrm{dis}}} \right) \cdot \frac{\Delta t}{E_{\mathrm{TST}}^{\max}} \tag{29}$$

where $SOC_{\mathrm{TST}}(t)$ represents the state of charge of the TST at time t, $P_{\mathrm{TST}}^{\mathrm{ch}}(t)$ and $P_{\mathrm{TST}}^{\mathrm{dis}}(t)$ are the thermal energy charging and discharging rates at time t. Similar to the HST, the self-discharge factor $\sigma_{\mathrm{TST}} = 0$, as self-discharge effects are also typically negligible for thermal storage in well-insulated systems. $\eta_{\mathrm{TST}}^{\mathrm{ch}}$ and $\eta_{\mathrm{TST}}^{\mathrm{dis}}$ represent the TST charging and discharging efficiency factors, while $E_{\mathrm{TST}}^{\max}$ represents the maximum capacity of the TST.

3.2. Objective function

The objective functions are defined by the unique operational characteristics of zero-carbon airport microgrids, where aircraft electric charging and hydrogen refuelling dominate the airport energy demand. These demands vary across airports of different scales and operational intensities, often reaching hundreds of megawatts even with only regional aircraft [46]. To accommodate such electric and hydrogen demands, airport microgrids typically incorporate large-scale PV installations, which introduce inherent output fluctuations. For hydrogen-powered aircraft, airport energy infrastructure is further expanded with on-site electrolysers for local hydrogen production, and fuel cells for hydrogen-to-electricity conversion. Waste heat from fuel cell is recovered via thermal energy storage for subsequent utilization. Such airport microgrids create complex energy conversion processes and tight coupling across electricity, hydrogen, and thermal networks. The complexity of multi-energy interactions in airport microgrids presents significant challenges for long-term stable energy dispatch. To address this, this study incorporates operational risk metrics for each energy network (electrical, thermal, and hydrogen) as optimization objectives, thereby enhancing the system's ability to maintain continuous energy balance. Furthermore, an innovative demand shifting strategy for aircraft electric charging and hydrogen refuelling is also introduced, enabling redistribution of these large, time-bound loads within allowable time windows. Given the considerable magnitude of aircraft energy demands, such shifting can significantly impact power exchange with the external grid, motivating a flexibility objective to optimize power exchange and support grid services.

The proposed multi-objective optimization framework integrates three objectives: minimizing economic energy dispatch cost, reducing operational risk across multi-energy networks, and enhancing grid flexibility. The economic objective ensures cost-effective operation by minimizing daily operational expenses, the risk objective mitigates potential instabilities across electrical, thermal, and hydrogen networks, and the flexibility objective, defined as reducing grid purchase, strengthens grid auxiliary service capability. A weighted optimization framework balances trade-offs among these objectives, allowing system operators to adapt priorities to operational needs, seasonal variations, or emergency scenarios, thereby enhancing the airport microgrid's adaptability, resilience and cost effectiveness.

The inherent variability of solar irradiance introduces certain fluctuations into PV power output, necessitating a robust probabilistic modelling framework for stable system operation. To effectively capture these variations, a scenario-based modelling approach is adopted. Let ξ denote the random variable representing variations in the system, primarily the variable PV output. A set of representative scenarios $\{\xi_s, s = 1, \ldots, S\}$ is generated using Latin Hypercube Sampling (LHS). Specifically, for each scenario ξ_s, sampling process is first performed using its Cumulative Distribution Function (CDF), which indicates the likelihood of the variable falling at or below a certain value [54]. The cumulative distribution function $F(G)$ is divided into N equal probability intervals, where

$$P(G_k < G < G_{k+1}) = \frac{1}{N} \tag{30}$$

The corresponding CDF value is calculated as

$$F(G_k) = \frac{1}{N} r_n + \frac{k-1}{N} \tag{31}$$

where r_n follows a uniform distribution N (0,1). The actual sample values for scenario ξ_s are then obtained through inverse transform sampling, expressed as

$$G_k = F^{-1} \left(\frac{1}{N} r_n + \frac{k-1}{N} \right) \tag{32}$$

The generated scenarios $\{\xi_s\}$ are organized into an $N \times P$ matrix, where P represents the number of time periods under consideration. While LHS provides good space-filling properties in the sample space, to improve numerical conditioning and reduce computational burden, a two-stage reduction process is implemented.

First, the Gram-Schmidt (GS) orthogonalization process is applied to minimize linear dependencies between scenarios and enhance the numerical stability of the scenario matrix. Given the smooth and unimodal nature of daily PV output profiles, this orthogonalization preserves the essential temporal patterns while improving computational tractability.

Subsequently, a Synchronous Backward Reduction (SBR) technique is also employed to obtain a representative subset while preserving the statistical properties of the original set. The distance between scenarios ξ_i and ξ_j is quantified using the Euclidean norm [54]:

$$d(i,j) = \sqrt{\sum_{t=1}^{T} \left(\xi_{it} - \xi_{jt} \right)^2} \tag{33}$$

where ξ_{it} and ξ_{jt} represents the value of scenario i and j at time t, respectively.

This distance-based reduction approach ensures that extreme scenarios (e.g., days with exceptionally high irradiance or heavily overcast conditions) are preserved, as they typically lie at the boundary of the scenario set in Euclidean space and maintain large distances from other scenarios. The algorithm preferentially eliminates scenarios in dense regions of the sample space, thereby maintaining scenario diversity and capturing the full range of PV variability critical for robust system operation.

Each scenario ξ_s is assigned a corresponding probability weight ω_s, where

$$\sum_{s=1}^{S} \omega_s = 1 \tag{34}$$

The objective function is then formulated to minimize the expected value across all scenarios, expressed as:

$$\min E[f(x,\xi)] = \sum_{s=1}^{S} \omega_s [TC(x,\xi_s) + OPR(x,\xi_s) - GF(x,\xi_s)] \tag{35}$$

where $TC(x,\xi_s)$ represents the system operation cost under scenario ξ_s; $OPR(x,\xi_s)$ denotes the operational risk of the electricity-thermal-hydrogen energy networks under scenario ξ_s; and $GF(x,\xi_s)$ indicates the grid flexibility assessment under scenario ξ_s.

The proposed probability-based modelling approach effectively captures the stochastic characteristics of PV output while maintaining computational efficiency. This optimization framework is particularly suitable for the multi-objective optimization of airport microgrid systems, as it enables the simultaneous balancing of system economics, operational security, and flexibility under variable renewable energy generation in multi-energy networks.

3.2.1. Operational cost

The economic objective function for the day-ahead optimal problem is expressed as follows, where TC represents the total cost of operating the microgrid over T time periods, the objective function is represented in Eq. (36), The specific formula for each part of objective function is shown in Eq. (37)–(45).

$$\min TC(x,\xi_s) = \sum_{t=1}^{T} \sum_{n=1}^{N_1} C_{\mathrm{OM}}\left(P_n^{t,\xi_s}\right) + \sum_{t=1}^{T} \times \sum_{n=1}^{N_2} C_{\mathrm{eav}}\left(P_n^{t,\xi_s}\right) + \sum_{t=1}^{T} \left[C_{aging}^{t,\xi_s} + C_{grid}^{t,\xi_s} + C_{el}^{t,\xi_s} + C_{H_2}^{t,\xi_s} + C_{Heat}^{t,\xi_s}\right] + C_{demand}^{\xi_s} \tag{36}$$

$$C_{\mathrm{OM}}\left(P_n^{t,\xi_s}\right) = K_{\mathrm{om}_n} P_n^{t,\xi_s} + C_{\mathrm{az}_n} r(1+r)^{L_n} * \frac{P_n^{t,\xi_s}}{26280(1+r)^{L_n} - 1} \tag{37}$$

where cost of equipment maintenance and operation for the n th unit is denoted by $C_{\mathrm{OM}}()$, P_n^{t,ξ_s} represents the power generate by the equipment, and N_1 is the number of equipment in the microgrid; K_{om_n} denotes the maintenance cost factor of unit power output for equipment n, C_{az_n} is the unit capacity investment costs for equipment n, L_n denotes the expected lifetime, r is the annual growth rate of depreciation, the list of equipment is included as $n = \mathrm{PV; HFC; EL; TST; HST}$.

$$C_{\mathrm{eav}}\left(P_{grid}^{t,\xi_s}\right) = \left(\mathrm{Kec}_{\mathrm{CO_2}} + \mathrm{Kec}_{\mathrm{SO_2}} + \mathrm{Kec}_{\mathrm{NO_X}}\right) \times P_{grid}^{t,\xi_s} \tag{38}$$

The emissions cost of the unit is shown in Eq. (38), where $C_{\mathrm{eav}}\left(P_{grid}^{t,\xi_s}\right)$ denotes the cost of emissions associated with the operation of the equipment. The hydrogen fuel cell in the system only uses green hydrogen and do not emit polluting gases, while other local generation equipment including PV panel, electrolyser and energy storage equipment are also considered operating without pollution, therefore the emissions cost is only induced by the external grid in this study. P_{grid}^{t,ξ_s} represents the power purchased from the external grid at time t. $\mathrm{Kec}_{\mathrm{CO_2}}$; $\mathrm{Kec}_{\mathrm{SO_2}}$; $\mathrm{Kec}_{\mathrm{NO_X}}$ are the unit cost coefficients for emissions associated with grid power generation.

The battery aging cost represents a significant component of the total system operation cost. For each time interval, the degradation cost is calculated based on the effective discharge throughput [54]:

$$C_{aging}^{t,\xi_s} = \frac{C_{BESS}^{unit} \cdot E_{BESS}^{max} \cdot d_{eff}^{t,\xi_s}}{E_{life}} \tag{39}$$

where C_{BESS}^{unit} represents the unit investment cost of the BESS, d_{eff}^{t,ξ_s} is the effective ampere-hour consumption considering both DoD and discharge rate effects, and E_{life} is the total baseline throughput in ampere-hours.

The total battery degradation cost over the optimization horizon T is:

$$C_{aging}^{total,\xi_s} = \sum_{t=1}^{T} C_{aging}^{t,\xi_s} \tag{40}$$

This degradation cost is incorporated into the overall system operation cost objective, incentivizing operational strategies that balance immediate energy arbitrage benefits against long-term battery life preservation.

The electrolyser contributes to the total system operation cost through startup-related expenses, which reflect the operational wear and efficiency losses during transient states:

$$C_{el}^{t,\xi_s} = C_{startup,cold} \cdot u_{startup,cold}^{t,\xi_s} + C_{startup,hot} \cdot u_{startup,hot}^{t,\xi_s} \tag{41}$$

where $u_{startup,cold}^{t,\xi_s}$ and $u_{startup,hot}^{t,\xi_s}$ are binary variables indicating cold and hot startup events at time t, $C_{startup,cold}$ and $C_{startup,hot}$ represent cold and hot startup costs respectively.

Cold startup costs are significantly higher due to extended power consumption during the startup sequence and increased thermal stress on system components. Hot startup costs are relatively lower as the system maintains residual thermal energy, enabling faster transition to production state with minimal auxiliary power requirements.

Eq. (42) denotes the cost or revenue associated with buying and selling electricity, where C_{pbuy}^{t} and C_{psell}^{t} denote the purchase price and sale price of the grid at time t, respectively. $P_{gridbuy}^{t,\xi_s}$ and $P_{gridsell}^{t,\xi_s}$ represent the interactive power exchange of the grid at time t.

$$C_{grid}^{t,\xi_s} = C_{pbuy}^{t} P_{gridbuy}^{t,\xi_s} - C_{psell}^{t} P_{gridsell}^{t,\xi_s} \tag{42}$$

Eq. (43) shows the cost for buying hydrogen through external hydrogen pipeline, C_{H_2} denotes the price of hydrogen, P_{H2buy}^{t,ξ_s} is the quantity of hydrogen purchased at time t.

$$C_{H_2}^{t,\xi_s} = C_{H_2} P_{H2buy}^{t,\xi_s} \tag{43}$$

Eq. (44) represents the cost for purchasing heat from the external district heating network. C_{Heat} denotes the unit price of thermal energy, $P_{Heatbuy}^{t,\xi_s}$ is the quantity of heat purchased at time t.

$$C_{Heat}^{t,\xi_s} = C_{Heat} \cdot P_{Heatbuy}^{t,\xi_s} \tag{44}$$

Apart from the typical cost elements associated with conventional multi-energy microgrids, airports featuring large-scale aircraft electrification are characterized by exceptionally high electricity consumption, which can impose significant stress on the upstream power grid during peak demand periods. To mitigate peak airport demand and reduce grid stress, demand charges are implemented as an economic incentive mechanism that encourages demand shifting and peak shaving behaviours. The demand charges are calculated based on the peak power demand during the optimization period, as expressed in Eq. (45):

$$C_{demand}^{\xi_s} = P_{peak} \cdot \tau_{demand} \tag{45}$$

where P_{peak} represents the maximum power demand over the selected day, and τ_{demand} denotes the demand tariff rate. The demand tariff is determined according to data regularly published by the National Energy System Operator (NESO) for Great Britain [60]. While several

European countries implement explicit demand-based tariffs, the UK employs a triad-based scheme where demand charges are determined based on the average peak power over the three highest half-hour periods of grid demand on specific days in winter. In this study, demand charges are simplified and defined as the peak demand of the selected day multiplied by the demand tariff for computational tractability.

3.2.2. *Multi-energy network operational risk*

Operational risk in power systems is typically defined as a comprehensive assessment of both the probability and severity of uncertainties during system operation. In this paper, we select three primary risk indicators for the airport multi-energy microgrid: electrical power imbalance, thermal power imbalance, and hydrogen power imbalance. Each of these imbalance indicators encompasses both positive and negative deviations. The final risk assessment is quantified by multiplying the power imbalances with their corresponding severity factors. The overall system operational risk is expressed in Eq. (46):

$$minOPR(x,\xi_s)=\sum_{i=1}^{T}\left(P_{out}^{i,\xi_s}\times S_{ev}\left(P_{out}^{i,\xi_s}\right)+Q_{out}^{i,\xi_s}\times S_{ev}\left(Q_{out}^{i,\xi_s}\right)+H_{out}^{i,\xi_s}\times S_{ev}\left(H_{out}^{i,\xi_s}\right)\right) \tag{46}$$

where *OPR* represents the total system operational risk and *T* is the system operation period. P_{out}^{i,ξ_s}, Q_{out}^{i,ξ_s}, and H_{out}^{i,ξ_s} represent the electrical, thermal, and hydrogen power imbalances at time *i*, respectively. $S_{ev}\left(P_{out}^{i,\xi_s}\right)$, $S_{ev}\left(Q_{out}^{i,\xi_s}\right)$, and $S_{ev}\left(H_{out}^{i,\xi_s}\right)$ denote the severity factors for the power imbalances in these energy networks, respectively.

The severity factor represents the degree of severity when power imbalances occur in the system. In this paper, the severity of electrical, thermal, and hydrogen power imbalances is characterized by the function shown in Eq. (47):

$$\begin{cases} S_{ev}\left(P_{out}^{i,\xi_s}\right)=\dfrac{exp\left(A_i{}^*\left(P_{out}^{i,\xi_s}\right)+B_i\right)-1}{C_i} \\ S_{ev}\left(Q_{out}^{i,\xi_s}\right)=\dfrac{exp\left(\alpha_i{}^*\left(Q_{out}^{i,\xi_s}\right)+\beta_i\right)-1}{\delta_i} \\ S_{ev}\left(H_{out}^{i,\xi_s}\right)=\dfrac{exp\left(\varepsilon_i{}^*\left(H_{out}^{i,\xi_s}\right)+\theta_i\right)-1}{\mu_i} \end{cases} \tag{47}$$

where A_i, B_i, C_i are the fitting parameters for the electrical power imbalance severity function; α_i, β_i, δ_i are the fitting parameters for the thermal power imbalance severity function; and ε_i, θ_i , μ_i are the fitting parameters for the hydrogen power imbalance severity function. The term *exp*() represents the exponential function with base *e*.

Based on Eq. (47), it can be observed that the severity factor exhibits exponential growth with the increase in power imbalance, which significantly impacts the objective function. This exponential relationship effectively serves as a penalty term, naturally constraining the further escalation of operational risks in the airport multi-energy microgrid. Such a mechanism is particularly crucial for maintaining the stable operation of the integrated electricity-thermal-hydrogen network.

3.2.3. *Flexibility potential of airport microgrid*

The system flexibility is quantified by comparing the grid interaction patterns between two optimization scenarios. Let P_{grid}^{b,ξ_s} denote the total daily grid power exchange between the airport microgrid and the utility grid when the objective function only include operational costs and risks; P_{grid}^{flex,ξ_s} represents the aggregate grid power exchange over the scheduling period when all three objectives are optimized. The flexibility is quantified as:

$$\max GF(x,\xi_s)=\left|P_{grid}^{b,\xi_s}-P_{grid}^{flex,\xi_s}\right| \tag{48}$$

The flexibility can be classified into two types: positive flexibility and negative flexibility. Positive flexibility represents a reduction in grid power purchases compared with baseline scenario, while negative flexibility indicates an increase in grid power purchases. In this study, positive flexibility is adopted as the primary flexibility indicator, reflecting microgrid's capability to reduce dependency on external grid power. The mathematical formulations for positive and negative flexibility are expressed as follows:

$$\max GF_{\text{pos}}(x,\xi_s)=P_{grid}^{b,\xi_s}-P_{grid}^{flex,\xi_s} \tag{49}$$

$$\max GF_{\text{neg}}(x,\xi_s)=P_{grid}^{flex,\xi_s}-P_{grid}^{b,\xi_s} \tag{50}$$

3.3. *Constraints*

3.3.1. *Multi-energy network balance and external interaction constraints*

The operation of the airport microgrid is constrained by energy balances across electricity, thermal, and hydrogen networks. The electrical balance constraint is expressed as:

$$P_{eleload}^{t,\xi_s}+P_{el}^{t,\xi_s}+P_{gridsell}^{t,\xi_s}+P_{BESS,cha}^{t,\xi_s}=P_{PV}^{t,\xi_s}+P_{fc}^{t,\xi_s}+P_{BESS,dis}^{t,\xi_s}+P_{gridbuy}^{t,\xi_s} \tag{51}$$

where P_{el}^{t,ξ_s} represents power consumed by electrolyser, and the power output of HFC is indicated by P_{fc}^{t,ξ_s}. $P_{BESS,cha}^{t,\xi_s}$ and $P_{BESS,dis}^{t,\xi_s}$ are the charging and discharging power of the BESS at time *t*, while $P_{gridbuy}^{t,\xi_s}$ and $P_{gridsell}^{t,\xi_s}$ denotes the power purchase from and sale to the utility grid, respectively.

The thermal network balance constraint is given by:

$$P_{Hload}^{t,\xi_S}=P_{TST}^{t,\xi_S}+Q_{fc}^{t,\xi_S}+P_{Heatbuy}^{t,\xi_S} \tag{52}$$

The power balance constraint of the thermal network is described by Eq. (52), including the waste heat recovered through heat exchanger Q_{fc}^{t,ξ_S}, external thermal power purchase $P_{Heatbuy}^{t,\xi_S}$, the thermal load of the terminal building P_{Hload}^{t,ξ_S}, and the thermal power output or input of the TST P_{TST}^{t,ξ_S}.

The hydrogen network balance follows:

$$P_{H_2Load}^{t,\xi_S}+P_{fc,H_2}^{t,\xi_S}=P_{H2}^{t,\xi_S}+P_{HST}^{t,\xi_S}+P_{H_2buy}^{t,\xi_S} \tag{53}$$

The power output or input of the HST is denoted as P_{HST}^{t,ξ_S}, and the hydrogen demand at time *t* is $P_{H_2Load}^{t,\xi_S}$. P_{fc,H_2}^{t,ξ_S} represents the hydrogen consumption power of the HFC, while $P_{H_2buy}^{t,\xi_S}$ is the hydrogen consumption power of the electrolyser. $P_{H_2buy}^{t,\xi_S}$ is the hydrogen power purchased from the pipeline at time *t*.

In this study, the airport microgrid is modelled using a single-bus structure without considering detailed internal network physics. Specifically, electrical network constraints such as voltage limits and line capacity, thermal network characteristics including heat losses and temperature gradients, and hydrogen network dynamics such as pressure variations and flow limitations are not explicitly modelled. This simplification is justified by the compact spatial scale of the airport microgrid, the short distribution distances involved, and the support from external utility networks that ensure stable operating conditions. The energy balance equations (Eq. (51)–(53)) therefore represent aggregated power flows at the system level rather than detailed network power flow calculations.

The interactions with external energy networks are further constrained by upper and lower bounds on power, hydrogen, and heat exchanges:

$$\begin{cases} P_{gridbuy}^{min} \le P_{gridbuy}^{t,\xi_s} \le P_{gridbuy}^{max} \\ P_{gridsell}^{min} \le P_{gridsell}^{t,\xi_s} \le P_{gridsell}^{max} \\ P_{H_2buy}^{min} \le P_{H_2buy}^{t,\xi_s} \le P_{H_2buy}^{max} \\ P_{Heatbuy}^{min} \le P_{Heatbuy}^{t,\xi_s} \le P_{Heatbuy}^{max} \end{cases} \tag{54}$$

3.3.2. *Dispatchable equipment power output constraints*

Dispatchable equipment such as fuel cells and electrolysers are constrained within minimum and maximum output ranges, expressed as:

$$P_n^{\min} \le P_n^{t,\xi_s} \le P_n^{\max}, n = \mathrm{HFC}, \mathrm{EL} \tag{55}$$

where $P_n^{\min}$ and $P_n^{\max}$ denote the minimum and maximum power output of equipment n, respectively.

Beyond these limits, electrolyser operation is also governed by the following technical and operational constraints to ensure realistic system behaviour [57]. Startup dynamics are modelled to capture both cold and hot processes, requiring proper durations and corresponding electrical consumption, which is formulated as:

$$\begin{cases} u_{on}^{t} + \sum\limits_{\tau=t-T_{cold}+1}^{t} u_{startup,cold}^{\tau} \le 1 \quad \forall t \in T \\ u_{standby}^{t} + \sum\limits_{\tau=t-T_{cold}+1}^{t} u_{startup,cold}^{\tau} \le 1 \quad \forall t \in T \\ u_{on}^{t} - u_{on}^{t-1} \le u_{startup,hot}^{t} + u_{startup,cold}^{t} + \sum\limits_{\tau=t-T_{cold}}^{t-1} u_{startup,cold}^{\tau} \quad \forall t \in T \\ P_{el,startup}^{t} = \dfrac{P_{startup,cold}}{T_{cold}} \sum\limits_{\tau=t-T_{cold+1}}^{t} u_{startup,cold}^{\tau} + P_{startup,hot} \cdot u_{startup,hot}^{t} \quad \forall t \in T \end{cases} \tag{56}$$

where T_{cold} represents the cold startup duration, ensuring that cold startup requires sustained operation for T_{cold} periods. These constraints ensures that the electrolyser can achieve proper cold and hot startup processes while consuming the corresponding power.

Electrolyser operating states are mutually exclusive, preventing simultaneous operation in production and standby modes, which is expressed as:

$$u_{on}^{t} + u_{standby}^{t} \le 1 \quad \forall t \in T \tag{57}$$

To ensure durability, a minimum load constraint is imposed since industrial electrolysers cannot maintain stable electrochemical reactions at very low current densities, leading to efficiency degradation:

$$P_{el,min} \cdot u_{on}^{t} \le P_{el,prod}^{t} \quad \forall t \in T \tag{58}$$

where $P_{el,min}$ represents the minimum stable operating load.

Hydrogen production is coupled to the active state of the electrolyser, formulated as:

$$m_{H_2}^{t} \le M \cdot u_{on}^{t} \quad \forall t \in T \tag{59}$$

where M is a sufficiently large constant, ensuring that hydrogen is only produced during the active operating state. Finally, the electrolyser thermal state is preserved to allow hot startup within $T_{cooldown}$, a defined cooldown duration after shutdown, which is represented by:

$$u_{startup,hot}^{t} \le \sum_{\tau=t-T_{cooldown}}^{t-1} u_{on}^{\tau} \quad \forall t \in T \tag{60}$$

3.3.3. *Constraints on energy storage systems*

Eq. (61) constrains the remaining energy capacity at any given time t to ensure operational feasibility within the system's physical limitations.

$$S_n^{\min} \le S_n^{t,\xi_s} \le S_n^{\max} \tag{61}$$

where $S_n^{\min}$ and $S_n^{\max}$ represent the minimum and maximum allowable capacity of the multi-energy storage systems, respectively.

During the energy dispatch process, the charging and discharging power of storage systems is constrained by both their permissible remaining capacity range and inherent technical limitations. The maximum charging and discharging power can be expressed as:

$$\begin{cases} 0 \leqslant P_{n,ch}^{t,\xi_s} \leqslant P_{n,ch\,max}^{t,\xi_s} = min\left\{ P_{n,max}^{ch}, \dfrac{\left[S_n^{max} - S_n^{t-1}(1-\sigma_n)\right]}{\eta_n^{ch}\Delta t} \right\} \\ 0 \leqslant P_{n,dis}^{t,\xi_s} \leqslant P_{n,dismax}^{t,\xi_s} = min\left\{ P_{n,max}^{dis}, \dfrac{\left[S_n^{t-1}(1-\sigma_n) - S_n^{min}\right]\eta_n^{dis}}{\Delta t} \right\} \end{cases} n = \mathrm{BESS}, \mathrm{HST}, \mathrm{TST} \tag{62}$$

where $P_{n,max}^{ch}$ and $P_{n,max}^{dis}$ are the maximum charging and discharging power of the multi-energy storage systems, respectively.

To enhance the participation of multi-energy storage systems in the dispatch of subsequent days, it is essential that their final capacity at the end of the current dispatch $S_n^{t=T}$ aligns with the initial capacity $S_n^{t=0}$. However, considering the large capacity of the storage tank and the flexibility of the energy system, a threshold value ψ_n is set in this study to reduce the computational complexity of optimization problem, the remaining capacity at the end of a day and initial capacity of the day are subject to the following constraints:

$$\frac{\left|S_n^{t=0} - S_n^{t=T}\right|}{S_n^{t=0}} \le \psi_n \tag{63}$$

3.3.4. *Aircraft charging and refuelling constraints*

Based on the predefined charging or refuelling power and duration for each aircraft described in Section 2.2.2, the following constraints must be satisfied in the charging and refuelling schedule optimization:

First, to ensure continuous charging or refuelling process, each aircraft can only be charged or refuelled once without interruption. The charging or refuelling status of aircraft i at time t is defined by a binary variable $x_{i,t}$. When the aircraft is being charged or refuelled, $x_{i,t}$ equals 1, otherwise, it equals 0. This continuous charging or refuelling requirement can be described as:

$$x_{i,t} = \begin{cases} 1, & \text{if } s_i \le t < s_i + T_{\mathrm{air}}^{i} \\ 0, & \text{otherwise} \end{cases} \quad \forall i \in N, \forall t \in T \tag{64}$$

where s_i represents the charging or refuelling start time of aircraft i, and

T_{air}^i denotes its required charging or refuelling duration.

Although Eq. (64) defines the charging status, the start time s_i is an implicit decision variable that requires additional constraints to define its feasible range, $t_i^{arr} \le s_i \le t_i^{dep} - T_{air}^i$. Excessive computational complexity is caused by formulating s_i as a continuous variable with nonlinear constraints linked to binary variables $x_{i,t}$, or by modelling each $x_{i,t}$ as an independent binary decision variable. In the latter approach, 200 aircraft over 72 time intervals at 20-min resolution would require up to 14,400 binary variables along with numerous logical constraints for continuity and exclusivity. To overcome this issue, the problem is reformulated by explicitly optimizing charging start time through discrete binary variables.

Binary decision variables are introduced to indicate when charging begins:

$$w_{i,s} = \begin{cases} 1, & \text{if aircraft } i \text{ starts charging at time } s \\ 0, & \text{otherwise} \end{cases} \quad \forall i \in N, \forall s \in T \tag{65}$$

The charging and refuelling scheduling problem is then expressed as:

$$\sum_{s=t_i^{arr}}^{t_i^{dep}-T_{air}^i} w_{i,s} = 1, \forall i \in N \tag{66}$$

where $w_{i,s} = 0, \forall i \in N, \forall s < t_i^{arr}$ or $s > t_i^{dep} - T_{air}^i$

This constraint ensures that each aircraft has exactly one charging or refuelling start time within its feasible window.

In addition, to guarantee a continuous and complete charging or refuelling process, it is necessary to ensure that once charging or refuelling begins at time s, it proceeds without interruption for the full duration T_{air}^i required by the aircraft type. Therefore, the charging or refuelling status $x_{i,t}$ is determined by the selected start time and only remain active throughout the charging or refuelling period, as expressed in Eq. (67):

$$x_{i,t} = \sum_{s \in \mathscr{S}_i(t)} w_{i,s}, \forall i \in N, \forall t \in T \tag{67}$$

where $\mathscr{S}_i(t) = \left\{ s : s \le t < s + T_{\text{air}}^i, t_i^{arr} \le s \le t_i^{dep} - T_{air}^i \right\}$ represents the set of start time that would result in charging or refuelling at time t.

Meanwhile, to prevent system overload, the total power demand from all aircraft at any time must not exceed the system capacity:

$$\sum_i \left(P_i^{air} x_{i,t} \right) \le P_{\max}^{air}, \forall t \in T \tag{68}$$

where P_i^{air} is the power demand of aircraft i and $P_{\max}^{air}$ represents the maximum system power capacity.

These constraints collectively ensure that each aircraft receives one continuous charging or refuelling session while maintaining the system power demand within its capacity limit throughout the optimization period.

4. Solution methodology

4.1. Model linearization

The optimization model for airport energy management involves two types of nonlinear terms that need to be addressed: the absolute value terms and the part-load efficiency curves of energy storage and conversion equipment. We propose systematic linearization approaches for each type of nonlinearity to transform the model into a MILP formulation.

It should be emphasized that in the aircraft charging and refuelling constraints, the relationship between $w_{i,s}$ and $x_{i,t}$ in Eq. (65) represents a logical constraint rather than a bilinear term. Since the charging power for each aircraft is predetermined as a constant (as shown in Eq. (11)), the constraint states that if charging starts at time s when $w_{i,s} = 1$, the aircraft must maintain its charging status during the interval $\left[s, s + T_{\text{air}}^i - 1\right]$.

This logical relationship is expressed as:

$$w_{i,s} = 1 \Rightarrow x_{i,t} = 1, \forall t \in \left[s, s + T_{\text{air}}^i - 1\right] \tag{69}$$

Given that $x_{i,t} \in \{0, 1\}$ represents a binary charging status and the charging power is a predetermined constant, this constraint can be implemented without introducing bilinear terms through:

$$x_{i,t} \ge w_{i,s} \quad t \in \left[s, s + T_{\text{air}}^i - 1\right], \forall i, s \tag{70}$$

Additionally, to prevent charging activity outside the selected charging period, the following constraint is imposed:

$$x_{i,t} \le \sum_{s \in \mathscr{S}_i(t)} w_{i,s}, \forall i, t \in T \tag{71}$$

This constraint serves as an upper bound: when no charging start time covers time slot t, the summation equals 0, forcing $x_{i,t} = 0$; when exactly one start time covers time slot t, the summation equals 1, allowing $x_{i,t} = 1$.

Together, Eqs. (70) and (71) ensure that $x_{i,t} = 1$ if and only if time t falls within a selected charging period. With predetermined constant charging powers, the formulation remains a standard MILP problem without requiring Big-M linearization, thus preserving numerical stability and avoiding relaxation gaps typically associated with Big-M methods.

The energy conversion devices in the multi-energy microgrid exhibit nonlinear efficiency characteristics that vary significantly with operating load levels. To maintain the linearity of the optimization model while accurately capturing these nonlinear behaviours, we employ piecewise linear (PWL) approximation based on convex combinations with Special Ordered Set of Type 2 (SOS2) constraints.

The core principle of our linearization approach is to represent any operating point as a convex combination of predefined breakpoints. For a nonlinear efficiency function $\eta(P/P^{max})$, we select N_{bp} breakpoints at load levels $\left\{\rho_1, \rho_2, \ldots, \rho_{N_{bp}}\right\}$ with corresponding efficiencies $\left\{\eta_1, \eta_2, \ldots, \eta_{N_{bp}}\right\}$. The efficiency at any operating point is then approximated as:

$$\eta_t = \sum_{k=1}^{N_{bp}} \lambda_{k,t} \cdot \eta_k \tag{72}$$

where the weight variables $\lambda_{k,t}$ form a convex combination satisfying:

$$\sum_{k=1}^{N_{bp}} \lambda_{k,t} = 1, \lambda_{k,t} \ge 0, \forall k, t \tag{73}$$

These constraints ensure that the weights are non-negative and sum to unity, defining a valid convex combination. However, allowing all $\lambda_{k,t}$ to be simultaneously non-zero would result in arbitrary weighted averages rather than piecewise linear interpolation. To enforce proper PWL behaviour, we impose the SOS2 constraint:

$$\text{sos2}\left(\lambda_{1,t}, \lambda_{2,t}, \ldots, \lambda_{N_{bp},t}\right) \tag{74}$$

This constraint restricts at most two adjacent λ variables to be non-zero, ensuring that the operating point is represented as a convex combination of only two consecutive breakpoints. Mathematically, if the operating load falls between breakpoints k and $k+1$, then:

$$\lambda_{k,t} + \lambda_{k+1,t} = 1, \lambda_{j,t} = 0 \quad \forall j \notin \{k, k+1\} \tag{75}$$

This formulation achieves linear interpolation between adjacent breakpoints while maintaining the convexity properties of the approximation. The operating power is expressed as convex combinations:

$$P_t = \sum_{k=1}^{N_{bp}} \lambda_{k,t} \cdot P_k \tag{76}$$

This convex combination approach transforms the nonlinear efficiency curves into a set of linear constraints, while the SOS2 constraints ensure that the approximation follows the piecewise linear segments rather than arbitrary convex hull relaxations. The method preserves the computational advantages of linear programming while maintaining high fidelity to the original nonlinear characteristics, particularly in the typical operating regions where breakpoints are strategically concentrated.

Another source of nonlinearity comes from the absolute value terms. Due to the scale of the model and the number of variables involved, the absolute value terms in our airport energy management model present significant non-linear challenges. For any absolute value term $|x|$, we introduce an auxiliary variable k to represent the absolute value. The

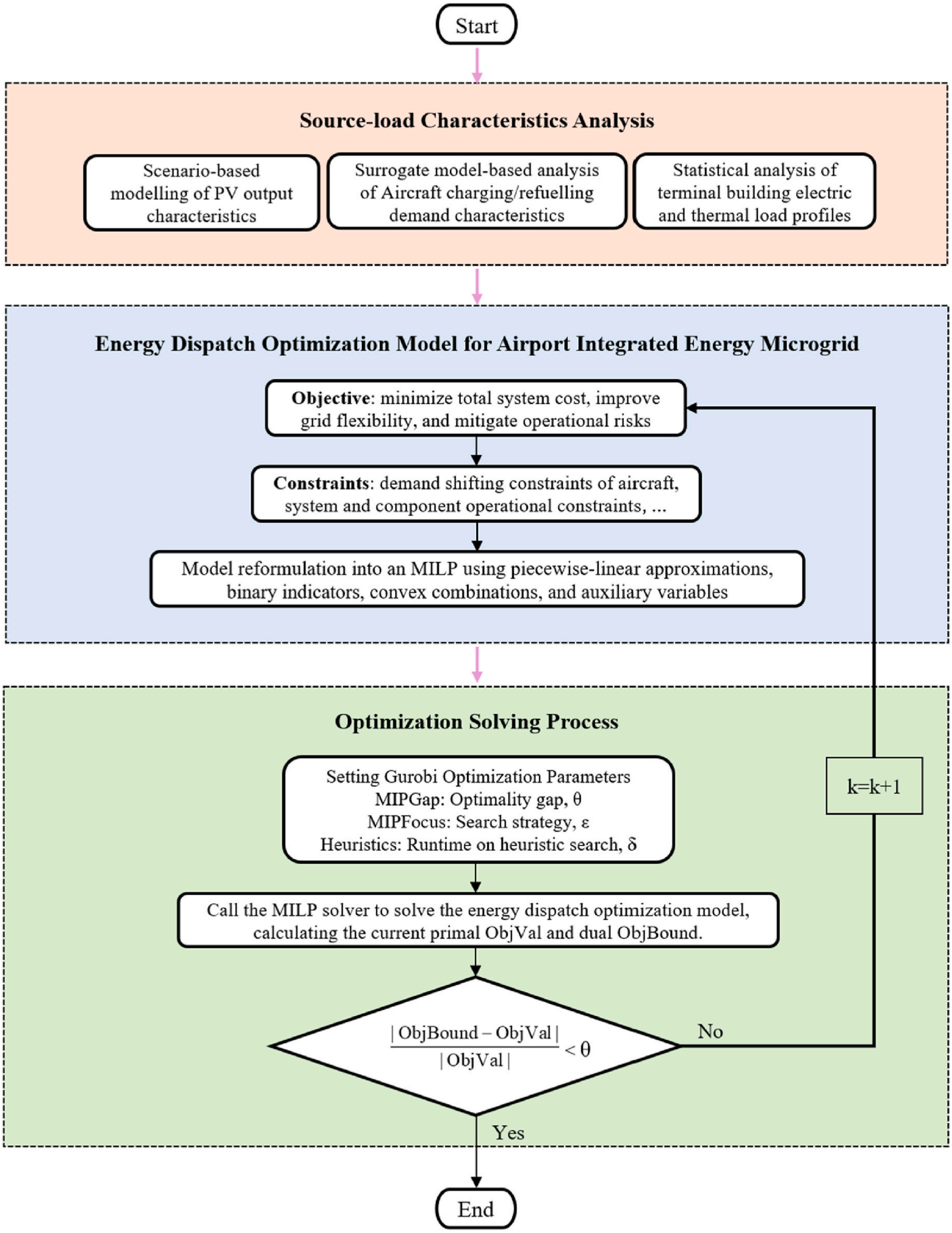

Fig. 4. Optimization framework for airport microgrid energy dispatch.

relationship $|x| = k$ can be equivalently transformed into a set of linear constraints:

$$\begin{cases} k \geq x \\ k \geq -x \end{cases} \tag{77}$$

where k is a non-negative variable representing $|x|$. This transformation is exact because in the objective minimization, k will always take the value $|x|$ at optimality due to the minimization pressure.

The proposed linearization approaches introduce additional variables and constraints. In absolute value linearization, continuous variables k and paired inequality constraints are added, while in the SOS2-based piecewise linearization, weight variable $\lambda_{k,t}$ and SOS2 constraints are introduced. Although these transformations increase the problem dimension, the resulting MILP formulation is typically more computationally tractable for commercial optimization solvers such as Gurobi or CPLEX than original nonlinear formulation, and it preserves the logical structure of the formulation while improving computational efficiency.

4.2. Solution process

The proposed optimization framework for airport microgrid energy dispatch comprises three primary phases, as depicted in Fig. 4. The initial phase analyzes source-load characterization, where scenario-based techniques capture PV generation variability, surrogate models analyse aircraft energy requirements during charging/refuelling operations, and statistical methods establish electric and thermal demand patterns for the terminal building.

Subsequently in the second phase, the energy dispatch optimization model is formulated with multiple objectives: minimizing overall operational expenditure, enhancing power grid flexibility, and reducing system-wide operational risks. This model integrates aircraft demand shifting capabilities alongside comprehensive operational constraints for microgrid equipment. The resulting nonlinear formulation is transformed into a computationally efficient MILP formulation through piecewise linearization, binary variable introduction, and convex reformulation techniques.

In the optimization solving phase, key Gurobi solver parameters are configured to balance computational efficiency with solution quality. The embedded MILP solver iteratively computes both primal and dual bounds until the relative optimality gap satisfies the prescribed tolerance, thereby guaranteeing convergence to a high-quality solution within acceptable computational time.

5. Results and analysis

The proposed methodology is demonstrated through a case study based on Manchester Airport, UK. The system comprises various energy supply equipment sized to meet the airport's electrical, thermal, and hydrogen demands. A large-scale PV installation with 50 MW capacity serves as the primary renewable energy source. The energy conversion equipment includes a 100 MW hydrogen fuel cell system with a load-dependent thermoelectric ratio and a 100 MW hydrogen electrolysis plant to facilitate bidirectional energy conversion between the hydrogen and electrical networks. Notably, the electrolyser employs a multi-state transition model to more accurately evaluate the performance and economics of on-site hydrogen production.

The multi-energy storage systems are designed with coordinated capacity to ensure reliable energy supply. A BESS with 150 MWh capacity is implemented alongside a TST rated at 50 MWh and a HST with 150-ton capacity. The BESS incorporates battery degradation costs to reflect the economic impact of cycling-induced aging. For all storage systems, the initial SoC is set at 0.5 and ψ is fixed at 0.01, with operational constraints limiting the SoC between 0.2 and 0.9 to ensure system longevity and operational stability.

The airport terminal energy demand is estimated using the modelling and analysis method presented in Ref. [61], which provides statistically analysed daily energy consumption patterns for a representative sample of administrative offices, including key end-use facilities such as lighting, heating, ventilation, and air conditioning (HVAC), and plug loads, which represent the primary electrical and thermal energy-consuming equipment servicing airport terminals [62]. The demand profiles are subsequently scaled by the airport's annual passenger volume to reflect airport-specific energy demand, enabling a data-driven approximation that captures both operational characteristics and system scale. To accommodate varying energy costs throughout the day, the system operates under a time-of-use electricity purchase pricing structure. Specifically, rates are set at 0.07 £/kWh during off-peak hours from 00:00–07:00. The rate increases to 0.15 £/kWh during mid-peak periods from 10:30 to 16:00 and from 21:00 to midnight. The highest rate of 0.20 £/kWh applies during peak periods from 7:00–10:30 and from 16:00–21:00. The electricity sale price to the external grid is set at 0.09 £/kWh based on the current electricity market rates. Heat purchase from external sources is priced at 0.08 £/kWh, accounting for clean heat requirements in district heating via heat pumps and other renewable technologies.

Despite the lack of a standardized hydrogen market mechanism, considering the potential correlation between hydrogen production costs and electricity prices due to the electricity-intensive nature of electrolysis, we adopt a hydrogen pricing strategy aligned with the peak-valley structure of time-of-use electricity tariffs. This approach is consistent with current green hydrogen production practices, which predominantly rely on large-scale electrolysis [63]. To reflect practical market dynamics and pricing delays, hydrogen prices are modelled with a 1-h lag relative to electricity prices. Other economic parameters are provided in the Appendix.

The stochastic nature of PV generation is modelled using beta distribution parameters derived from historical illumination intensity data, with mean and variance values given in Ref. [64]. 10 representative PV generation scenarios, obtained using scenario generation and reduction methods, are illustrated in Fig. 5(a), with their corresponding probability distributions shown in Fig. 5(b).

The developed multi-energy microgrid optimization framework, which coordinates the energy dispatch between future airport infrastructures and zero-emission aircraft, is implemented in MATLAB 2024b. The resulting MILP problem is solved using the Gurobi optimization solver. All computations are performed on a MacBook equipped with an M4 Pro chip and 48 GB RAM.

5.1. Statistical analysis of electric and hydrogen-powered aircraft energy demands at airport

To comprehensively understand the flight operations and energy demand variations at the selected airport, flight data throughout the year 2023 are collected and analysed. The dataset includes flight duration and aircraft type information for each flight. Different aircraft models are assigned specific weighting factors to account for their varying energy demands. The equivalent flight duration for each flight operation is calculated using Eq. (78), and the total equivalent flight hours for each time period is determined by Eq. (79):

$$t_{eq,i} = t_{actual,i} \times W_{type,i} \tag{78}$$

$$T_{eq,p} = \sum_{i \in F_p} t_{eq,i} \tag{79}$$

where $t_{eq,i}$ is the equivalent flight duration of flight i, $t_{actual,i}$ represents the actual flight duration of flight i, $W_{type,i}$ is the weighting factor corresponding to the aircraft type of flight i, $T_{eq,p}$ is the total equivalent flight hours during time period p , and F_p denotes the set of flights operating during time p.

Using Eq. (78) and Eq. (79), the daily cumulative equivalent flight

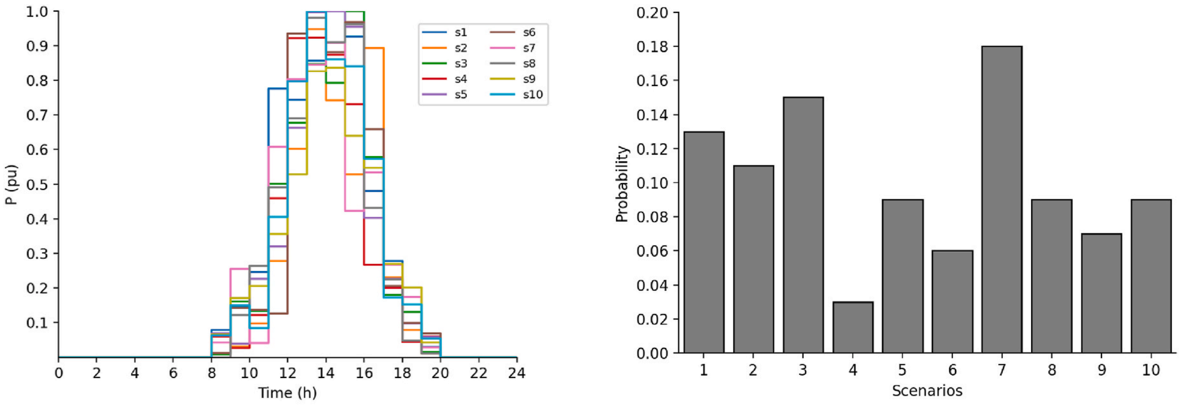

(a) (b)

Fig. 5. (a) Representative daily PV generation scenarios; (b) Probability of each scenario.

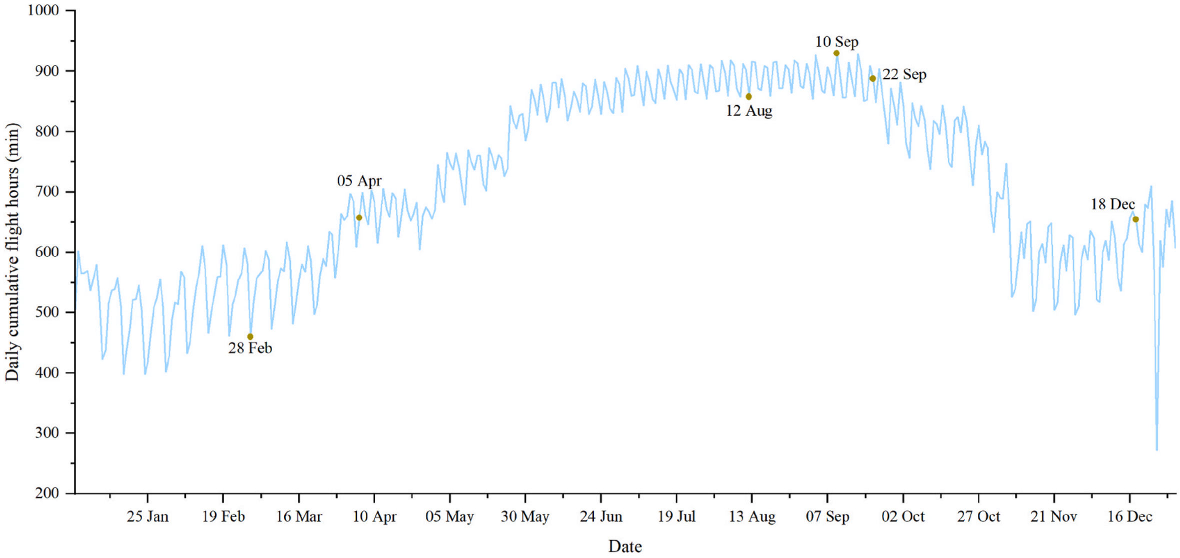

Fig. 6. Daily cumulative flight hours and distribution of clustered typical days in 2023.

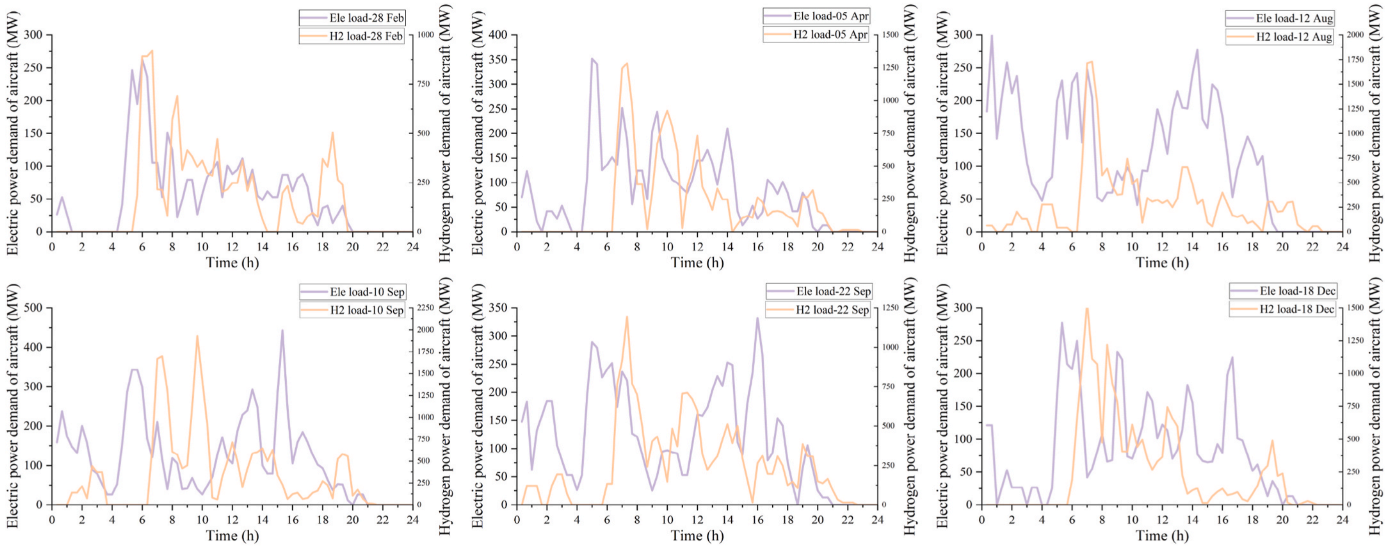

Fig. 7. Electric and hydrogen power demands of aircraft at representative days.

hours are calculated. The k-medoids clustering method is then applied to identify representative daily demand patterns, resulting in six typical clusters. As shown in Fig. 6, these representative days are well-distributed throughout the dataset, with a particularly higher concentration around September aligning with the airport's busiest operations. The temporal distribution of the clustered typical days effectively captures both seasonal variations and peak operation periods, validating the effectiveness of the clustering approach.

In the proposed energy dispatch optimization strategy, aircraft demands are shifted in real-time based on airport microgrid needs during the optimization process. This means the aircraft's total demand profile is not fixed beforehand. To facilitate analysis of aircraft demand pattern variations, we considered a scenario where aircraft do not perform demand shifting. Instead, each aircraft begins charging or refuelling immediately upon landing. (If an aircraft arrived prior to the selected day, charging or refuelling is completed at the corresponding time before its scheduled departure). The duration for charging or refuelling is determined by the settings for each aircraft type as specified in Table A1. By fixing the charging or refuelling start time, the electric and hydrogen power demands for aircraft operations on six representative days (February 28, April 5, August 12, September 10, September 22, and December 18) are obtained, as shown in Fig. 7.

From Fig. 7, it can be observed that each of the six representative days exhibits unique characteristics in both electric and hydrogen power demands. In particular, aircraft energy demands in August and September are significantly higher than those on other days, aligning with the increased air traffic during the UK's summer travel peak. Specifically, September 10 exhibits the highest peak electric demand; however, its demand profile fluctuated more significantly compared to August 12. The latter maintained a relatively stable high-level demand throughout the day, peaking at around 300 MW. The hydrogen demand profile presents a different pattern, with September 10 showing both the highest peak value and average value. Since medium and large aircraft primarily rely on hydrogen-powered propulsion, these trends suggest that while both days experience high airport traffic, August 12 accommodates more small aircraft, whereas September 10 generally hosts more large aircraft.

February 28 presents the lowest aircraft energy demands among the selected days. Notably, the electric and hydrogen demand profiles for this day follow relatively similar trends, generally showing a gradual decrease from a morning peak, with no flight operations during the night. These demand patterns reflect a significantly lower proportion of hydrogen-powered aircraft on this day, with operations mainly dominated by hybrid hydrogen -electric aircraft, resulting in a noticeable correlation between electric and hydrogen demands. In contrast, December 18 displays an almost opposite demand pattern. Aside from the early morning period with few flights, electric and hydrogen demands often changed inversely throughout the day, possibly indicating a limited presence of medium-sized hybrid hydrogen-electric aircraft. With fewer total flight operations, an increase in battery-powered aircraft likely results in a decrease in hydrogen-powered aircraft, contributing to this inverse relationship between these two types of energy demands.

The analysis reveals significant variations in demand patterns and magnitudes across these representative days, reflecting the dynamic nature of aircraft energy requirements at airport throughout the year. Overall, given that the electric charging demands are comparable in scale between all-electric aircraft and the battery-supplied portion of hybrid hydrogen-electric aircraft, the electric demand variations across different days show complex trends with no significant regular patterns, primarily influenced by the actual flight schedules of each day. Hydrogen demands, however, exhibit a very clear peak from morning to midday. While the peak magnitudes vary across days, the timing of these peaks remains relatively consistent, indicating that large hydrogen-powered aircraft, which constitute the majority of hydrogen demand at the selected airport, mainly operate during arrival and departure in this period.

Among these typical days, April 5 is selected as the representative day for detailed energy dispatch analysis of the airport microgrid in the following chapter. This is due to its distinctive demand characteristics, with a relatively balanced distribution of all three aircraft types, making it an ideal case for demonstrating the airport microgrid's capability in managing sharp demand variations and coordinating multiple energy sources. Additionally, its moderate flight volume and peak demand levels represent a balanced scenario that can effectively illustrate the typical operation patterns of the proposed energy management strategies.

5.2. *Analysis of airport energy dispatch results*

To comprehensively evaluate the impact of different optimization objectives on the energy dispatch results, five cases are designed to progressively incorporate various system features and objectives:

Case 1: Only operational cost minimization; aircraft demand shifting and PV variability are not considered.

Case 2: Only operational cost minimization; aircraft demand shifting allowed, PV variability not considered.

Case 3: Operational cost and risk minimization; aircraft demand shifting and PV variability considered.

Case 4: Operational cost minimization and power grid flexibility maximization; aircraft demand shifting and PV variability considered.

Case 5: Comprehensive optimization: operational cost minimization, operational risk minimization, and power grid flexibility maximization; aircraft demand shifting and PV variability considered.

The energy dispatch results for the electrical, thermal, and hydrogen networks are presented in Figs. 8–12, while Table 1 illustrates the relative changes in the three optimization objectives compared to Case 1.

In Case 1, where aircraft demand shifting strategy is not adopted, the electric demand exhibits a significant peak of approximately 350 MW shortly after 5 a.m., as shown in Fig. 8(a). The magnitude of the demand exceeds the capacity of the originally designed grid power exchange capacity for the airport microgrid, necessitating a specific increase in the maximum allowable power purchase limit for this case. Despite the off-peak electricity tariff during early morning hours, the hydrogen demand within the system is still met through external hydrogen purchase due to the coinciding low hydrogen prices and minimal hydrogen aircraft refuelling demand during this period, making hydrogen purchase more economically favourable than on-site production. Similar to aircraft electric demands, the hydrogen demand of the aircraft also cannot be optimized based on system characteristics, resulting in significant peak hydrogen demands. To accommodate these large peaks, the hydrogen import capacity are assumed to be adequately sized in Case 1. As shown in Fig. 8(c), this adaptation of system constraints leads to a dispatch pattern that heavily relies on external hydrogen purchase rather than utilizing the integrated hydrogen storage system, reflecting the hydrogen network's preference for direct energy supply when facing inflexible high demands. The fuel cell output varies in response to electricity and hydrogen price differentials. Notably, during 7–8 AM, electricity prices have risen to peak tariff levels while hydrogen prices remain at their daily minimum due to the 1-h lag, resulting in near-maximum fuel cell output to capitalize on this price arbitrage, as evident in Fig. 8(a) and (b).

With the adoption of demand shifting strategy in Case 2, the peak demand significantly decreased to approximately 150 MW, while demand levels increased during periods that has low charging demand in Case 1, effectively achieving peak shaving and valley filling potential, as depicted in Fig. 9(a). Specifically, the system maximizes power purchases during the 0–7 AM low-price period to meet both aircraft charging and battery storage charging demands. Beyond the morning peak, demand shifting results in increased aircraft energy demands during midday low-price periods and reduced demands during high-

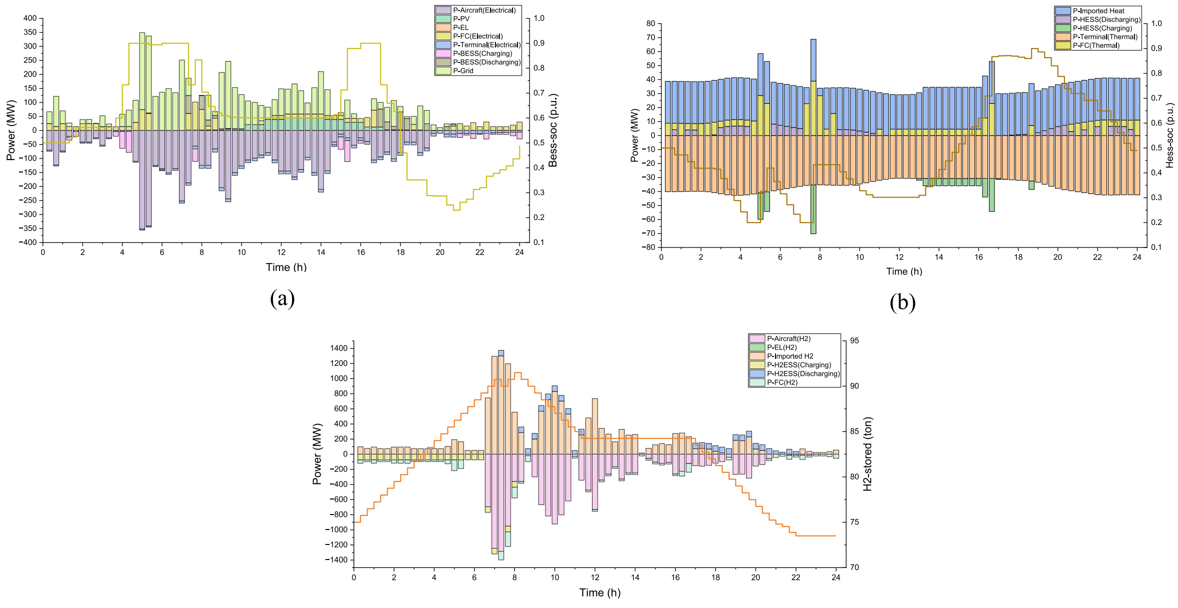

(a) (b)

(c)

Fig. 8. Energy dispatch results under Case 1: (a) power network, (b) thermal network, and (c) hydrogen network.

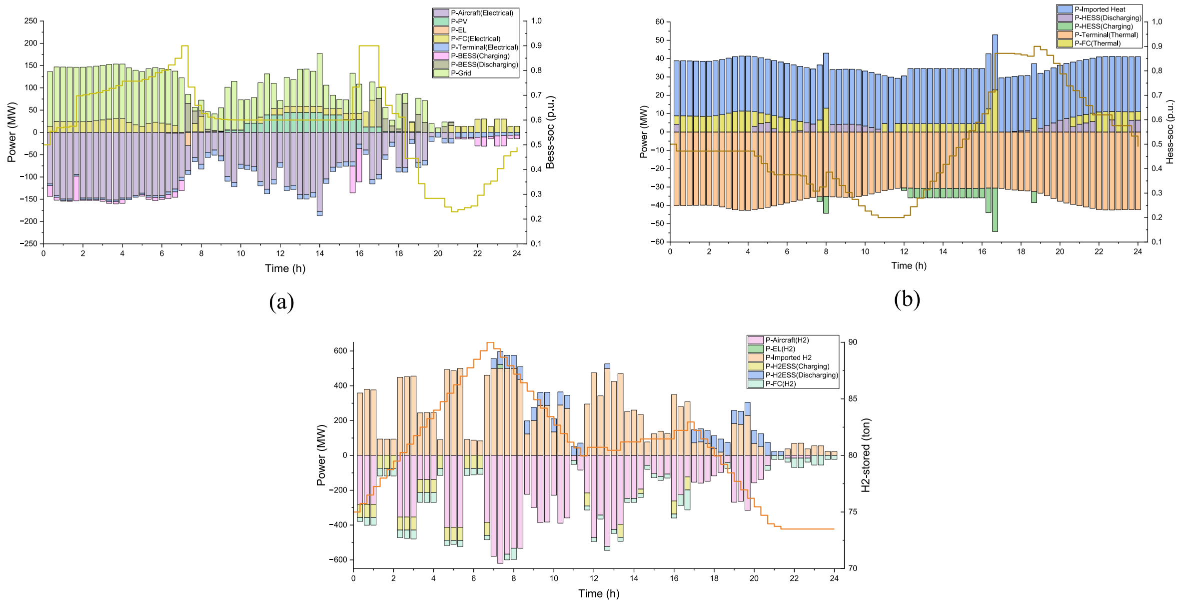

(a) (b)

(c)

Fig. 9. Energy dispatch results under Case 2: (a) power network, (b) thermal network, and (c) hydrogen network.

price time. Battery storage provides additional support during peak electricity price periods and high aircraft demand intervals, reducing high-price power purchases from upper grid. As shown in Table 1, this demand shifting strategy can reduce total costs by over 340,000 £. Unexpectedly, the electrolyser operates briefly between 7 and 8 a.m. despite unfavourable costs, as hydrogen prices are still at their lowest while electricity costs have risen to peak levels. This unusual operation is actually driven by peak hydrogen demand from aircraft refuelling requirements, necessitating on-site production to supplement insufficient external supply and ensure service reliability. According to Fig. 9 (b), thermal storage operation becomes less intensive due to the more stable fuel cell thermal output. Notably, hydrogen storage is utilized more frequently, absorbing excess hydrogen during off-peak pricing periods and releasing it during peak demand and high-price periods, with nighttime recharging to meet storage operational constraints, as demonstrated in Fig. 9(c).

In Case 3, where operational risks are constrained, the power network demonstrates a more pronounced risk reduction compared to the hydrogen and thermal networks. Specifically, as shown in Fig. 10, fuel cell operation becomes more frequent and intensive compared to the cost-minimization scenario in Case 2. Notably, in power network energy dispatch, fuel cells generate power even during periods when both electricity and hydrogen prices are high, indicating that the system starts to compromise economic efficiency to achieve risk mitigation, as shown in Fig. 10(a), while changes in thermal and hydrogen networks remain relatively modest. This differential response can be attributed to

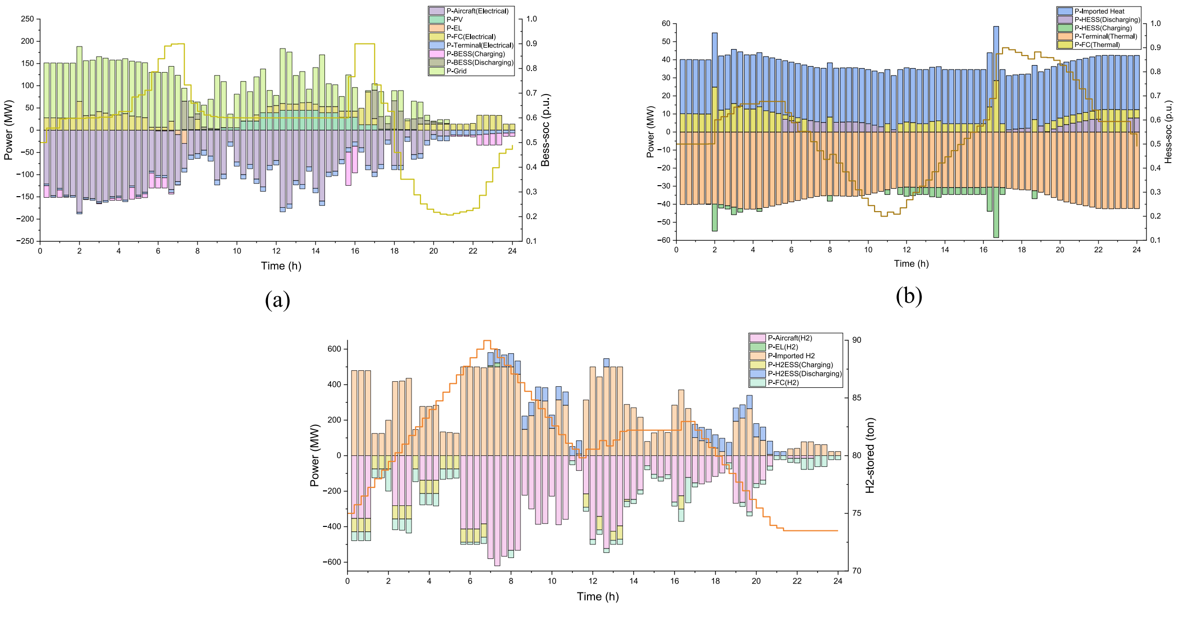

(a) (b) (c)

Fig. 10. Energy dispatch results under Case 3: (a) power network, (b) thermal network, and (c) hydrogen network.

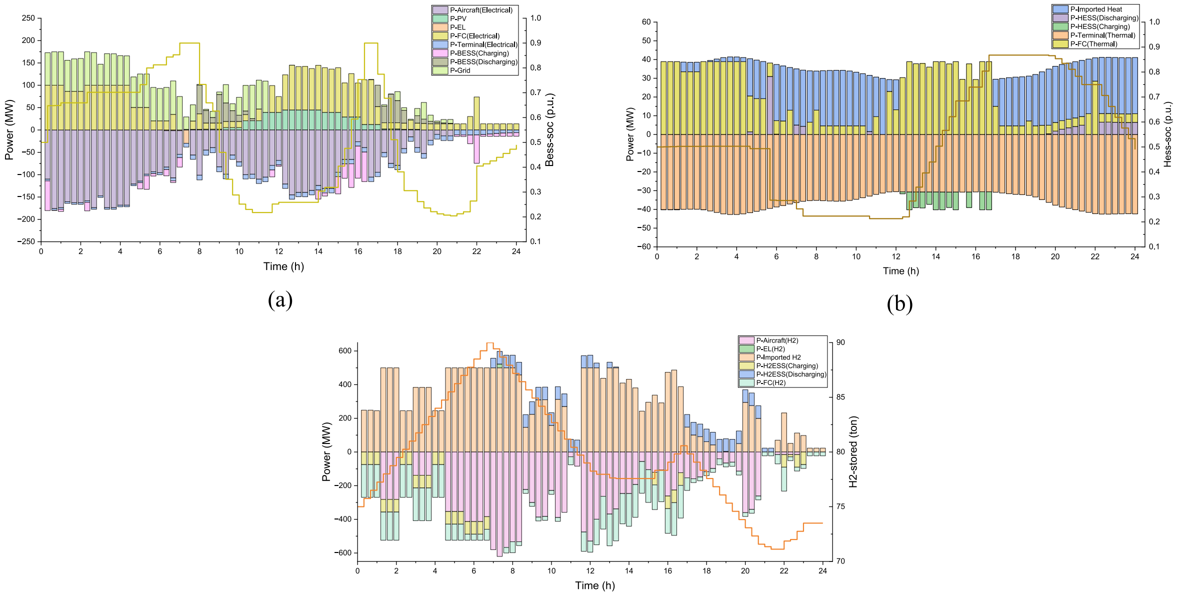

(a) (b) (c)

Fig. 11. Energy dispatch results under Case 4: (a) power network, (b) thermal network, and (c) hydrogen network.

the greater variety and quantity of dispatchable power equipment in the electrical network, combined with the demand shifting capability of electrical aircraft demands, which collectively enhance its risk management flexibility.

In contrast, the thermal network primarily serves terminal building's heating loads, which are fixed loads and therefore lack shifting flexibility. Additionally, despite the availability of external heat purchase from district heating networks, due to the inherent coupling between fuel cell heat recovery and thermal storage, the thermal network's dispatchable energy supply equipment often responds passively to variations in thermal supply. Similarly, the hydrogen network encounters limitations in risk reduction due to minimal active utilization of hydrogen storage, as discussed in the previous chapter. Moreover, according to the proposed aircraft recategorization strategy, hydrogen-powered aircraft are typically larger models with correspondingly higher energy demands, resulting in greater impact on the airport microgrid. Consequently, to maintain stable system operation while preserving economic efficiency, the optimization solution always tends to retain higher operational risks in both the hydrogen and thermal networks when feasible.

To enhance positive grid flexibility in Case 4, the electrical network significantly reduces morning low-price power purchases, as illustrated in Fig. 11(a), with high-output fuel cell generation covering the remaining electrical load. Hydrogen demand is primarily met through external purchase, with minor contributions from hydrogen storage during high-price periods. Compared to Case 2, midday electrical power

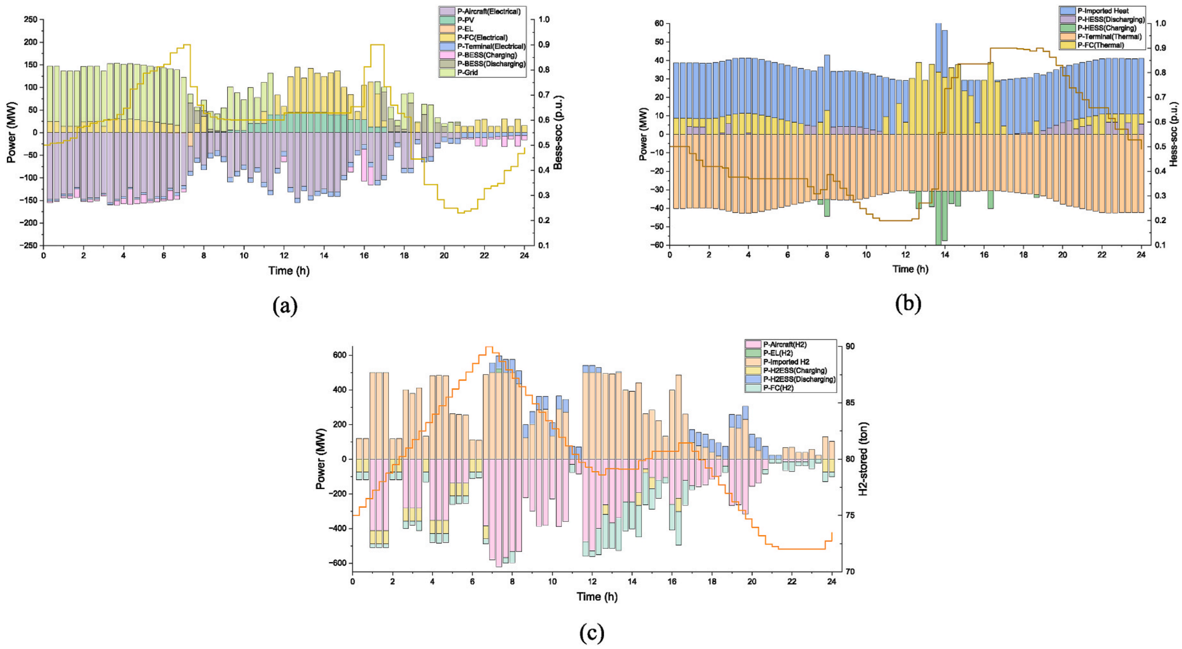

Fig. 12. Energy dispatch results under Case 5: (a) power network, (b) thermal network, and (c) hydrogen network.

Table 1
Variation of optimization objectives across different cases.

	Case 2	Case 3	Case 4	Case 5
Overall cost increment	£ −346425.83	£ 14375.22	£ 83941.95	£ 97734.76
Operation risk reduced by	/	63.21 %	/	38.28 %
Grid flexibility increased by	/	/	29.4 %	16.5 %

purchase reductions are compensated by battery storage discharge and fuel cell generation, particularly during peak solar irradiance periods with low electric demand when the system achieves complete energy self-sufficiency. However, frequent high-load fuel cell operation substantially increases external hydrogen purchase, thereby elevating overall system operating costs. The absence of power sales to the external grid indicates that, under current pricing and objective weights, the revenue potential does not offset the overall cost impact.

Case 5 represents a comprehensive balance of all optimization objectives. To achieve better economic performance, the system retains large-scale power purchases during off-peak morning periods, while midday loads are entirely supplied by fuel cells and PV generation, significantly enhancing system flexibility, though remaining below Case 4 levels. Operational risk shows significant reduction (38.28 %) but also remains higher than the comparison scenario Case 3 where grid flexibility is not considered, as shown in Fig. 12(a) and Table 1. Total system costs reach their maximum across all cases, reflecting the trade-offs required to simultaneously satisfy risk constraints and provide grid flexibility while maintaining cost efficiency. More precisely, this substantial cost increase results from the diminished weight of the economic objective in the objective function, as the system simultaneously accommodates network operational risk constraints while maintaining considerable grid flexibility.

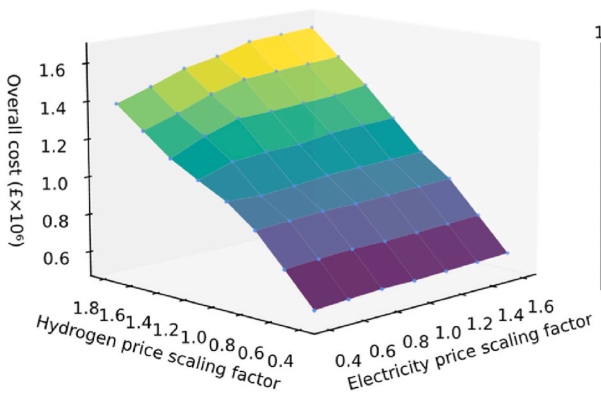

Fig. 13. Sensitivity analysis of energy prices on system total cost.

5.3. *Sensitivity analysis of energy prices on system performance*

To comprehensively investigate the relationship between the three optimization objectives proposed in this study, a sensitivity analysis is conducted to examine how energy prices affect the airport microgrid's total operating cost, network operational risks, and power grid flexibility. All other parameters remain consistent with those in Case 5 of the previous section, with the energy dispatch optimization considering all three objectives simultaneously, as illustrated in Figs. 13–14 and 16.

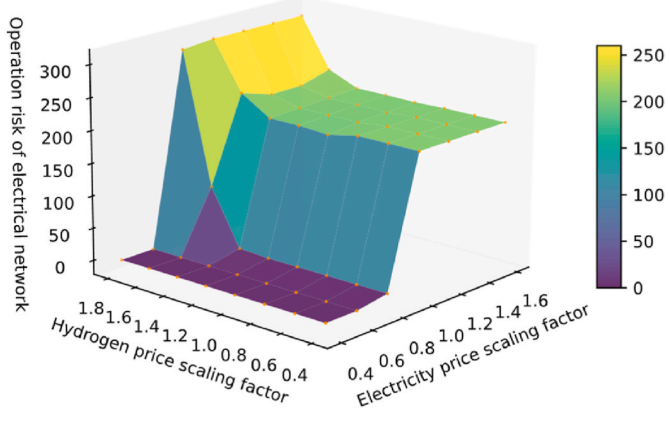

Fig. 14. Sensitivity analysis of energy prices on operation risk of power network.

The airport microgrid's total operating cost exhibits a clear trend of monotonic increase with rising electricity and hydrogen prices, as shown in Fig. 13. Notably, the cost increase rate is substantially higher with respect to hydrogen price variations compared to electricity price changes, indicating a significantly higher hydrogen utilization in the system. This observation aligns with the scales of electric and hydrogen demands shown in Fig. 7, where hydrogen demands constitute a larger portion of the total energy consumption. When hydrogen prices rise across all periods, local hydrogen production from electrolyser becomes more economical than external purchase even during off-peak hours, significantly increasing grid electricity purchases. However, the marginal increase in total cost gradually diminishes with rising electricity prices, suggesting that the grid power purchase has already approached its upper limit at moderate electricity prices.

Given that the operational risk in power network demonstrates the highest parameter sensitivity among the three network risks, as evidenced by the preceding energy dispatch analysis, this section focuses specifically on investigating the dynamic characteristics of power network operational risks under varying energy prices. As shown in Fig. 14, when electricity prices are low (0.4–0.6 times the baseline price), the power network maintains nearly risk-free operation regardless of hydrogen price fluctuations. This occurs because the cost increment from increasing grid power purchase is lower than the penalty imposed by additional risk in the objective function at low electricity prices. In other words, flexible adjustment of grid power purchase alone can sufficiently manage potential operational risks when electricity prices are low. As electricity prices rise, operational risks begin to emerge when external hydrogen prices are also high. When electricity prices increase further (up to 1.6 times the baseline), power network operational risks rise significantly across all hydrogen price ranges, indicating that the cost impact of increased power purchase becomes more dominant in the objective function, leading the system to tolerate higher operational risks. Specifically, when hydrogen prices reach 1.6–1.8 times the baseline, risks increase dramatically due to electrolyser operating near its maximum capacity for extended periods, as shown in Fig. 15, substantially reducing their risk regulation capability. This situation is further intensified by higher electricity prices limiting grid power purchases, resulting in fewer flexible energy resources for adjustment. Notably, at intermediate hydrogen price levels, risks decrease slightly compared to lower hydrogen price scenarios. This unusual behaviour most likely results from specific combinations of multi-source power outputs rather than indicating a systematic trend.

The relationship between power grid flexibility and energy prices exhibits more complex patterns, as demonstrated in Fig. 16. To better understand how flexibility potential varies with energy prices, further analysis of daily power purchase patterns is required, comparing scenarios with and without flexibility objectives, as shown in Figs. 17–18. This analysis is essential since positive grid flexibility is defined as the difference in total power exchange with the main grid between scenarios with and without flexibility parameters in the objective function.

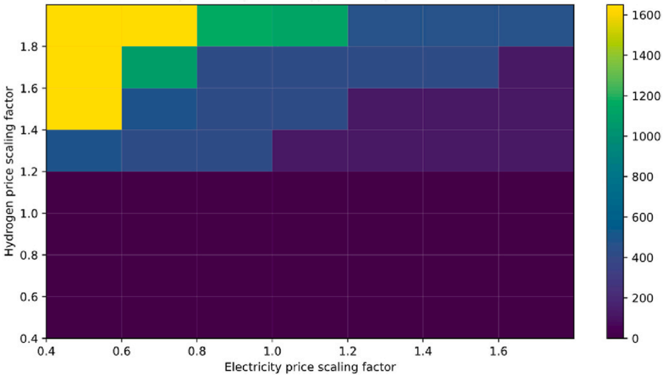

Fig. 15. Electrolyser energy consumption variations with energy prices.

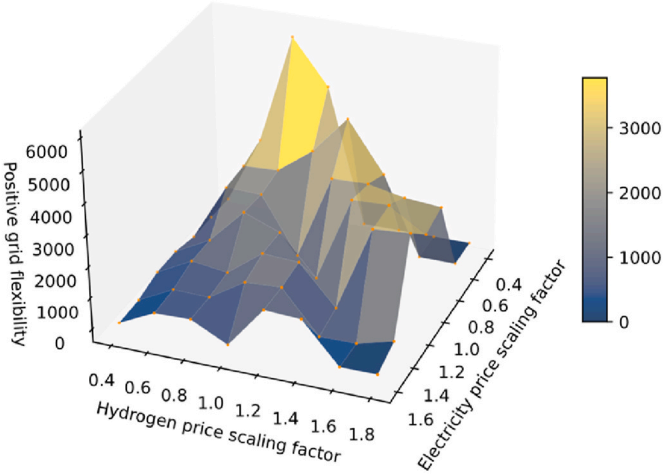

Fig. 16. Sensitivity analysis of energy prices on positive grid flexibility.

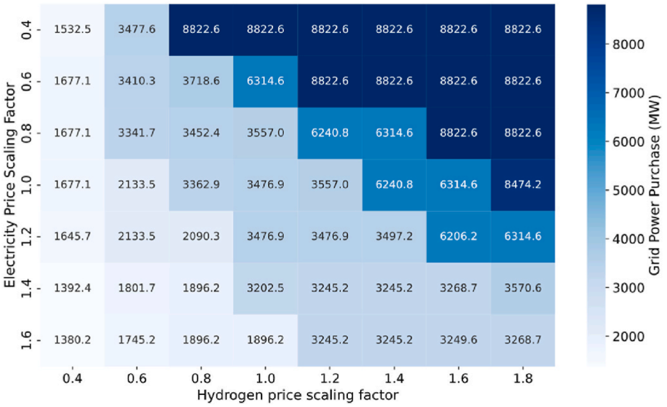

	0.4	0.6	0.8	1.0	1.2	1.4	1.6	1.8
0.4	1532.5	3477.6	8822.6	8822.6	8822.6	8822.6	8822.6	8822.6
0.6	1677.1	3410.3	3718.6	6314.6	8822.6	8822.6	8822.6	8822.6
0.8	1677.1	3341.7	3452.4	3557.0	6240.8	6314.6	8822.6	8822.6
1.0	1677.1	2133.5	3362.9	3476.9	3557.0	6240.8	6314.6	8474.2
1.2	1645.7	2133.5	2090.3	3476.9	3476.9	3497.2	6206.2	6314.6
1.4	1392.4	1801.7	1896.2	3202.5	3245.2	3245.2	3268.7	3570.6
1.6	1380.2	1745.2	1896.2	1896.2	3245.2	3245.2	3249.6	3268.7

Fig. 17. Grid power purchase variations with energy prices without considering grid flexibility.

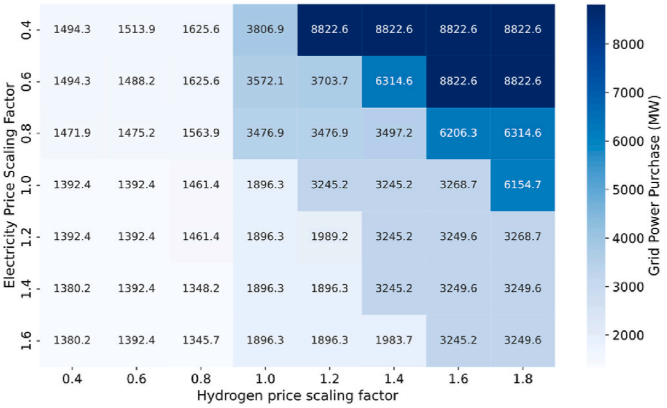

	0.4	0.6	0.8	1.0	1.2	1.4	1.6	1.8
0.4	1494.3	1513.9	1625.6	3806.9	8822.6	8822.6	8822.6	8822.6
0.6	1494.3	1488.2	1625.6	3572.1	3703.7	6314.6	8822.6	8822.6
0.8	1471.9	1475.2	1563.9	3476.9	3476.9	3497.2	6206.3	6314.6
1.0	1392.4	1392.4	1461.4	1896.3	3245.2	3245.2	3268.7	6154.7
1.2	1392.4	1392.4	1461.4	1896.3	1989.2	3245.2	3249.6	3268.7
1.4	1380.2	1392.4	1348.2	1896.3	1896.3	3245.2	3249.6	3249.6
1.6	1380.2	1392.4	1345.7	1896.3	1896.3	1983.7	3245.2	3249.6

Fig. 18. Grid power purchase variations with energy prices considering grid flexibility.

In the baseline scenario without flexibility constraints, grid power purchase is substantial at low electricity prices and decreases with rising prices. As hydrogen prices increase, the cost advantage of hydrogen production from electrolyser becomes more prominent, leading to increased power purchases. In contrast, the scenario prioritizing grid flexibility (Fig. 18) moderates power purchases even during low-price periods, with significant increases only at high hydrogen prices. This creates distinct differences in power purchase patterns between scenarios despite similar overall trends.

For instance, at the lowest electricity price (0.4 scaling factor of the baseline), baseline scenario power purchases reach peak levels when hydrogen prices are only 0.8 scaling factor of the baseline, significantly exceeding purchases at lower hydrogen prices. Meanwhile, the flexibility-oriented scenario does not reach similar levels until hydrogen prices increase to 1.2 scaling factor of the baseline, resulting in the substantial positive flexibility observed in this price range, as shown in Fig. 16. At low hydrogen prices, positive flexibility remains minimal because hydrogen production from electrolyser lacks cost advantages over external purchase, while fuel cells fully utilize low-cost hydrogen for maximum power generation, greatly reducing grid purchases in both scenarios and eliminating flexibility potential.

As hydrogen prices gradually increase, another critical characteristic emerges above moderate electricity price levels. At moderate electricity prices, cost considerations lead the airport microgrid to significantly increase power purchases only when hydrogen prices approach maximum levels. This leads to comparable power purchase levels between scenarios at moderate electricity and hydrogen prices, thereby limiting flexibility potential. Conversely, at high electricity prices, the incentive to avoid large-scale power purchases prevents significant increases in the baseline scenario even with high hydrogen prices, resulting in similar purchase levels between scenarios and limited flexibility provision. These findings emphasize the importance of optimal electricity and hydrogen price selection when aiming to maximize grid flexibility potential.

5.4. Impact assessment of electric and hydrogen aircraft integration ratio on system performance

To thoroughly investigate the impact of significant transition in energy demands from zero-emission aircraft on airport microgrid operations, the aircraft integration ratio of battery-electric, hydrogen-powered, and hybrid hydrogen-electric aircraft is systematically adjusted while adhering to actual flight scheduling requirements. Specifically, battery-powered regional aircraft are initially replaced by hydrogen fuel-cell models, while hybrid aircraft are converted to hydrogen-powered aircraft, thereby establishing an entirely hydrogen fleet. Subsequently, the transition toward increased electric demand begins with regional aircraft gradually being converted back to all-electric models. After fully reinstating all-electric regional aircraft, the hybridization ratio of hybrid aircraft is progressively increased until the overall electricity-to-hydrogen energy demand ratio across the entire fleet reaches approximately 3:7 [57].

To more accurately characterize the impact of aircraft energy demand changes on the operation of the airport microgrid, two indicators are defined as follows:

$$\lambda^{\text{ele}} = \frac{E_{\text{ele}}^{\text{total}}}{E_{\text{ele}}^{\text{total}} + E_{\text{hyd}}^{\text{total}}}, \lambda^{\text{hyd}} = \frac{E_{\text{hyd}}^{\text{total}}}{E_{\text{ele}}^{\text{total}} + E_{\text{hyd}}^{\text{total}}} \tag{80}$$

where $E_{\text{ele}}^{\text{total}}$ and $E_{\text{hyd}}^{\text{total}}$ represent the total electric and hydrogen energy demands of all aircraft, respectively. λ^{ele} and λ^{hyd} reflect the relative share of each energy type in the overall aircraft energy consumption.

As shown in Fig. 19(a), the total operating cost of the airport microgrid significantly declines as the proportion of electric demand increases. This trend is primarily attributed to the substantial hydrogen energy requirements of aircraft when electric demand is minimal. Under current pricing parameters, on-site electrolyser remains economically unviable except during peak demand periods. With most hydrogen sourced by external purchase at prices significantly exceeding electricity costs, high hydrogen demand results in substantial operating costs. Furthermore, when the aircraft integration ratio λ^{ele} is very low (less than 0.05), only regional aircraft undergo gradual electrification, resulting in minimal influence on energy dispatch and system operation in power network. This limited impact can be consistently observed in Fig. 19(a)–(c).

Fig. 19(b) illustrates that with the rapid increase in electric demand, aircraft demand shifting capabilities become fully leveraged, significantly enhancing the operational flexibility of the airport microgrid. Local energy generation operates actively and aligns closely with demand profiles, enabling the airport microgrid to provide considerable flexibility to the external grid. At an aircraft integration ratio λ^{ele} of 0.225, positive flexibility reaches its peak before rapidly declining. When λ^{ele} increases to 0.3, flexibility falls back to levels comparable to airport operations without any electric aircraft integration. This occurs because once electric demand exceeds the maximum output capability of local generation equipment, the system quickly shifts to relying on externally purchased electricity to maintain operational stability.

The impact of varying electricity-to-hydrogen energy demand ratio on airport microgrid energy dispatch is also manifest in the system's operational stability, as depicted in Fig. 19(c). When λ^{ele} exceeds 0.075, significant operational risks emerge in the power network, escalating rapidly while maintaining considerable margin from the allowable risk threshold. This indicates that airport microgrid equipment approach their maximum capability to collaboratively optimize energy dispatch during complex operational intervals. These intervals include high electricity price periods (07:00–10:00 and 16:00–21:00) and intensive aviation demand between 10:00–16:00. Efforts to enhance operational flexibility while controlling system costs have led to progressive instability in airport microgrid operations.

After λ^{ele} exceeds 0.15, following rapid growth, operational risk stabilizes at a relatively constant level. During this phase, operational risks also begin to emerge during low electricity-price intervals, but the lower purchasing cost brings reduced economic penalties. This allows the airport microgrid to utilize more grid power to balance operational

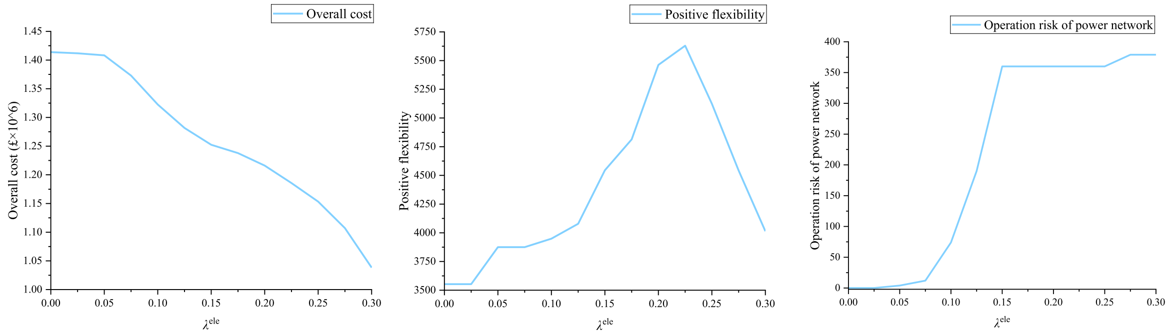

(a) (b) (c)

Fig. 19. Impact of electric aircraft integration ratio on system operation (a) Total cost; (b) Positive flexibility; (c) Operation risk of power network.

risks and costs, resulting in slower risk growth. However, it is foreseeable that if future technology trends enable further growth in aircraft electric demand, operational risks will soon approach critical thresholds, potentially constraining further aviation electrification without sufficient airport energy infrastructure.

6. Conclusions

This paper proposes a comprehensive energy dispatch optimization framework for electricity-thermal-hydrogen airport microgrid that explicitly incorporates aviation energy demands of electric, hydrogen, and hybrid hydrogen-electric aircraft. A multi-objective optimization model is developed to ensure that multi-energy supply dynamically responds to aviation demand, while optimizing overall system performance across economic, operational, and flexibility dimensions. Comparative scenario analysis under real-world operational requirements demonstrates that the proposed high-fidelity aircraft energy demand model effectively captures the flexibility potential of zero-emission aircraft powered by electricity and hydrogen while ensuring the current flight schedules are maintained. The results show that coordinated dispatch of energy generation, demand, and storage units can substantially improve both economic efficiency and grid support flexibility, with airport microgrid flexibility increased by 29.4 % and operational risk reduced by 63.2 %. Sensitivity analysis further highlights that under current energy prices and system parameters, an aircraft integration ratio λ^{ele} of approximately 0.225 delivers optimal overall system performance, balancing cost, stability, and flexibility, while maximizing grid services and keeping operational risks within acceptable thresholds.

Beyond these quantitative findings, this work also underscores the transformative impact of emerging aircraft technologies. The adoption of electric and hydrogen propulsion is expected not only to decarbonise aviation but also to fundamentally reshape air traffic patterns, increasing flight frequency across both regional and international routes. Such changes will intensify operational interdependencies among airports, highlighting the need for integrated, network-level studies. Therefore, future research will develop from single-airport analysis to multi-airport operations that examine inter-airport dynamics and the coupling between aviation electrification and energy networks.

CRediT authorship contribution statement

Bozheng Li: Writing – review & editing, Writing – original draft, Validation, Supervision, Software, Methodology, Investigation, Formal analysis, Data curation, Conceptualization. **Jinning Zhang:** Writing – review & editing, Visualization, Validation, Supervision, Methodology, Investigation, Conceptualization. **Xin Zhang:** Writing – review & editing, Validation, Supervision, Methodology, Funding acquisition, Conceptualization.

Declaration of competing interest

The authors declare that they have no known competing financial interests or personal relationships that could have appeared to influence the work reported in this paper.

Acknowledgement

This work was supported by the UK Engineering and Physical Sciences Research Council (EPSRC) through the New Investigator Award project “Aviation-to-Grid: Grid flexibility through multiscale modelling and integration of power systems with electrified air transport” (Grant No. EP/W028905/1).

Appendix

Table A1
Zero-emission aircraft mapping and energy supply duration assumptions

Origin aircraft type	Charging or refuelling duration
ATR 42 family ATR 72 family Bombardier Dash 8 Embraer E170 family Embraer E190 family Embraer ERJ family SAAB 340/2000 family	Battery-powered only 50-100 seats Charging duration: 40 min [65]
Airbus A220 family Airbus A300 family Airbus A310 family Airbus A320 family Boeing 737 family Boeing 757 family Boeing 767 family	Hybrid hydrogen-electric configuration: 160-230 seats [46] Charging/refuelling duration: 40 min
Airbus A330 family Airbus A340 family Airbus A350 family Boeing 787 family Boeing 777 family	Hydrogen-powered only 280-340 seats Refuelling duration: 60 min [4]

Table A2
Flight schedule arrivals [53].

Time	Flight	Origin	Airline	Aircraft
07:40	FR2071	Alicante (ALC)	Ryanair	B38M (EI-IKO)
07:45	FR1862	Cork (ORK)	Ryanair	B738 (EI-DWV)
07:48	EI631	Belfast (BHD)	Aer Lingus	AT76 (EI-FSL)
07:50	LM693	Isle of Man (IOM)	Loganair	AT76 (G-LMTE)
07:55	CX219	Hong Kong (HKG)	Cathay Pacific	A359 (B-LRT)
07:55	FR552	Dublin (DUB)	Ryanair	B738 (EI-DLW)
08:00	BA1370	London (LHR)	British Airways	A319 (G-EUPJ)

Table A3
Flight schedule departures [53].

Time	Flight	Destination	Airline	Aircraft
10:00	U22185	Geneva (GVA)	easyJet	A320 (G-EZTL)
10:05	FR2242	Bologna (BLQ)	Ryanair	B738 (9H-QCW)
10:05	VS73	Orlando (MCO)	Virgin Atlantic	A333 (G-VKSS)
10:05	SQ52	Houston (IAH)	Singapore Airlines	A359 (9V-SMS)
10:25	CX216	Hong Kong (HKG)	Cathay Pacific	A359 (B-LRT)
10:25	FR4007	Alicante (ALC)	Ryanair	B738 (EI-DCR)
10:25	GF4	Bahrain (BAH)	Gulf Air	B789 (A9C-FE)

Table A4
Key economic parameters of devices [7,27,37,54].

Devices	Installation cost	Maintenance cost (per year)
PV	850 £/kW	12.7 £/kW
Fuel Cell	403 £/kW	10.6 £/kW
Hydrogen tank	1260 £/kg	13.7 £/kW
Thermal tank	50 £/kWh	5.3 £/kWh
Battery storage	82 £/kWh	5.1 £/kWh
Electrolyser	546 £/kW	50.2 £/kW

Table A5
Other parameters of airport energy system [27,54,57].

Para	Value
$\mathrm{Kec}_{\mathrm{CO_2}}$	19.28 £/MWh
$\mathrm{Kec}_{\mathrm{SO_2}}$	2.67 £/MWh
$\mathrm{Kec}_{\mathrm{NO_x}}$	10.74 £/MWh
$L_{\mathrm{BSS,HFC}}$	10 years
L_{Other}	20 years
σ_{BESS}	0.01
$P_{el,min}$	$0.1P_{el,rated}$
$P_{el,stamdby}$	$0.03P_{el,rated}$

Data availability

Data will be made available on request.

References

[1] Gössling S, Humpe A, Fichert F, Creutzig F. COVID-19 and pathways to low-carbon air transport until 2050. Environ Res Lett 2021;16.

[2] Rupcic L, Pierrat E, Saavedra-Rubio K, Thonemann N, Ogugua C, Laurent A. Environmental impacts in the civil aviation sector: current state and guidance. Transport Res Transport Environ 2023;119:103717.

[3] Df Transport. Decarbonising transport: a better, greener Britain. Traffic engineering and control, vol. 51; 2021.

[4] Beddoes S, Foster M, James D, Kay E, Kay O, Shawki K. Aerospace technology institute-flyzero-zero-carbon emission aircraft concepts, vol. 2; 2022.

[5] Schwab A, Thomas A, Bennett J, Robertson E, Cary S. Electrification of aircraft: challenges, barriers, and potential impacts. 2021.

[6] Du H, Zhang X, Yu H. Design of high-energy-density lithium batteries: liquid to all solid state. eTransportation 2025/01/01;23.

[7] Guo Z, Zhang X, Balta-Ozkan N, Luk P. Aviation to grid: airport charging infrastructure for electric aircraft. 2020.

[8] Sawant V, Zambare P. DC fast charging stations for electric vehicles: a review. Energ Convers Econom 2024/02/01;5.

[9] Sripad S, Bills A, Viswanathan V, Sripad S, Bills A, Viswanathan V. A review of safety considerations for batteries in aircraft with electric propulsion. MRS Bull 2021;46(5). 2021–06–08;46.

[10] Yusaf T, Faisal Mahamude AS, Kadirgama K, Ramasamy D, Farhana K, Dhahad HA. Sustainable hydrogen energy in aviation – a narrative review. Int J Hydrogen Energy 2024;52:1026–45.

[11] Hughes C, Gear C, Milne K, Webb S, Debney D, Kumar N. Our vision for zero-carbon emission air travel. FlyZero General Report 2022.

[12] Cryogenic hydrogen fuel system and storage. Aerospace Technol Institute 2022.

[13] Government UK. Net zero strategy. Build Back Greener; 2021.

[14] Marciello V, Orefice F, Nicolosi F, Ciliberti D, Vecchia PD. Design of hybrid-electric aircraft with fault-tolerance considerations. Chin J Aeronaut 2023;36.

[15] Easa. SC E-19 special condition: electric/hybrid propulsion System. CRI Consultaticn Paper. Eurppean Union Aviation Safety Agency (EASA); 2021.

[16] Faa. hydrogen-Fueled aircraft safety and certification roadmap. Federal Aviation Administration (FAA); 2024.

[17] Easa. EASA certification roadmap on H2. EASA: European Union Aviation Safety Agency; 2024.

[18] Ahmadi S, Akgunduz A. Airport operations with electric-powered towing alternatives under stochastic conditions. J Air Transport Manag 2023;109:102392.

[19] Salihu AL, Lloyd SM, Akgunduz A. Electrification of airport taxiway operations: a simulation framework for analyzing congestion and cost. Transport Res Transport Environ 2021;97:102962.

[20] Liu Z, Wang Q, Sigler D, Kotz A, Kelly KJ, Lunacek M. Data-driven simulation-based planning for electric airport shuttle systems: a real-world case study. Appl Energy 2023;332:120483.

[21] Hasan S, Zeyad M, Ahmed SMM, Mahmud DM, Anubhove MST, Hossain E. Techno-economic feasibility analysis of an electric vehicle charging station for an International Airport in Chattogram, Bangladesh. Energy Convers Manag 2023; 293:117501.

[22] Guo Z, Lai CS, Luk P, Zhang X. Techno-economic assessment of wireless charging systems for airport electric shuttle buses. J Energy Storage 2023;64:107123.

[23] Hou B, Bose S, Marla L, Haran K. Impact of aviation electrification on airports: flight scheduling and charging. IEEE Trans Intell Transport Syst 2024;25.

[24] Doctor F, Budd T, Williams PD, Prescott M, Iqbal R. Modelling the effect of electric aircraft on airport operations and infrastructure. Technol Forecast Soc Change 2022;177:121553.

[25] Gnadt AR, Speth RL, Sabnis JS, Barrett SRH. Technical and environmental assessment of all-electric 180-passenger commercial aircraft. Prog Aero Sci 2019; 105.

[26] Eaton J, Naraghi M, Boyd JG. Regional pathways for all-electric aircraft to reduce aviation sector greenhouse gas emissions. Appl Energy 2024;373:123831.

[27] Guo Z, Li B, Taylor G, Zhang X. Infrastructure planning for airport microgrid integrated with electric aircraft and parking lot electric vehicles. eTransportation 2023;17:100257.

[28] Sreenath S, Sudhakar K, Yusop AF. Energy-exergy-economic-environmental-energo-exergo-enviroecono (7E) analysis of solar photovoltaic power plant: a case study of 7 airport sites in India. Sustain Energy Technol Assessments 2021;47: 101352.

[29] Sher F, Hazafa A, Marintseva K, Rasheed T, Ali U, Rashid T. Fully solar powered Doncaster Sheffield airport: energy evaluation, glare analysis and CO2 mitigation. Sustain Energy Technol Assessments 2021;45:101122.

[30] Sreenath S, Sudhakar K, Yusop AF, Solomin E, Kirpichnikova IM. Solar PV energy system in Malaysian airport: glare analysis, general design and performance assessment. Energy Rep 2020;6:698–712.

[31] Jiang M, Qi L, Yu Z, Wu D, Si P, Li P. National level assessment of using existing airport infrastructures for photovoltaic deployment. Appl Energy 2021;298: 117195.

[32] Goh HH, Suo W, Liang X, Zhang D, Dai W, Kurniawan TA. An adaptive energy management strategy for airports to achieve carbon neutrality by 2050 via waste, wind, and solar power. Front Energy Res 2024;12.

[33] Khalil M, Dincer I. Investigation of a new holistic energy system for a sustainable airport with green fuels. Sustain Cities Soc 2024;113:105624.

[34] Degirmenci H, Uludag A, Ekici S, Karakoc TH. Challenges, prospects and potential future orientation of hydrogen aviation and the airport hydrogen supply network: a state-of-art review. Prog Aero Sci 2023;141:100923.

[35] Farrokhi M, Javani N, Motallebzadeh R, Ebrahimpour A. Dynamic simulation and optimization of a novel energy system with hydrogen energy storage for hotel buildings. Energy 2022;257:124586.

[36] Zhao H, Xiang Y, Shen Y, Guo Y, Xue P, Sun W. Resilience assessment of hydrogen integrated energy system for airport electrification. IEEE Trans Ind Appl 2021;58 (2). 2812-1824.

[37] Xiang Y, Cai H, Liu J, Zhang X. Techno-economic design of energy systems for airport electrification: a hydrogen-solar-storage integrated microgrid solution. Appl Energy 2021;283:116374.

[38] Liu X, Li M, Liu X, Zhang T, Fu Z, Su Z. Quantifying energy flexibility potential of ground electric vehicles in an airport with real behavior data. Sustain Cities Soc 2024:105.

[39] Ollas P, Sigarchian SG, Alfredsson H, Leijon J, Döhler JS, Aalhuizen C. Evaluating the role of solar photovoltaic and battery storage in supporting electric aviation and vehicle infrastructure at visby airport. Appl Energy 2023;352.

[40] Alruwaili M, Cipcigan L. Airport electrified ground support equipment for providing ancillary services to the grid. Elec Power Syst Res 2022;211:108242.

[41] Guo Z, Zhang J, Zhang R, Zhang X. Aviation-to-Grid flexibility through electric aircraft charging. IEEE Trans Ind Inf 2022;18.

[42] Pu Y, Li Q, Luo S, Chen W, Breaz E, Gao F. Peer-to-Peer electricity-hydrogen trading among integrated energy systems considering hydrogen delivery and transportation. IEEE Trans Power Syst 2024;39.

[43] Shi M, Wang W, Han Y, Huang Y. Research on comprehensive benefit of hydrogen storage in microgrid system. Renew Energy 2022;194.

[44] Best I, Braas H, Orozaliev J, Jordan U, Vajen K. Systematic investigation of building energy efficiency standard and hot water preparation systems' influence on the heat load profile of districts. Energy 2020;197:117169.

[45] Guo Z, Zhang X, Zhang R. A multi-agent microgrid energy management solution for air transport electrification. 2021.

[46] Li B, Guo Z, Yuan Y, Zhang X. Study on the impact of aviation electrification on voltage deviation of the GB transmission system. IEEE 2022:1–6.

[47] Hull DG. Fundamentals of airplane flight mechanics. Berlin, Heidelberg: Springer; 2007.

[48] Doff-Sotta M, Cannon M, Bacic M. Predictive energy management for hybrid electric aircraft propulsion systems. IEEE Trans Control Syst Technol 2023;31.

[49] Jiang P, Zhou Q, Shao X. Surrogate-model-based design and optimization. 2020.

[50] Williams BA, Cremaschi S. Surrogate model selection for design space approximation and surrogatebased optimization. 2019.

[51] Fuhg JN, Fau A, Nackenhorst U. State-of-the-Art and comparative review of adaptive sampling methods for kriging, vol. 28. Archives of Computational Methods in Engineering; 2021.

[52] Drees L, Mueller M, Schmidt-Moll C, Gontar P, Zwirglmaier K, Wang C. Risk analysis of the EASA minimum fuel requirements considering the ACARE-defined safety target. J Air Transport Manag 2017;65:1–10.

[53] Airport Microgrid Flight Data. Electronic resource ed: github. 2025.

[54] Xiao H, Pei W, Dong Z, Kong L. Bi-level planning for integrated energy systems incorporating demand response and energy storage under uncertain environments using novel metamodel. CSEE J Power Energ Sys 2018;4:155–67.

[55] Xu L, Ruan X, Mao C, Zhang B, Luo Y. An improved optimal sizing method for wind-solar-battery hybrid power system. IEEE Trans Sustain Energy 2013;4.

[56] Decentralized multi-period economic dispatch for real-time flexible demand management. IEEE Trans Power Syst 2016;31.

[57] Virah-Sawmy D, Beck FJ, Sturmberg B. Ignore variability, overestimate hydrogen production – quantifying the effects of electrolyzer efficiency curves on hydrogen production from renewable energy sources. Int J Hydrogen Energy 2024/06/27: 72.

[58] Han J, Wang J, He Z, An Q, Song Y, Mujeeb A, et al. Hydrogen-powered smart grid resilience. Energ Convers Econom 2023/04/01;4.

[59] Duan L, Guo Z, Taylor G, Lai CS. Multi-objective optimization for solar-hydrogen-battery-integrated electric vehicle charging stations with energy exchange. Electronics 2023;12.

[60] NESO. Transmission network use of system tariffs for 2024/25. National energy system operator..

[61] Elkadeem MR, Kotb KM, Elmaadawy K, Ullah Z, Elmolla E, Liu B. Feasibility analysis and optimization of an energy-water-heat nexus supplied by an autonomous hybrid renewable power generation system: an empirical study on airport facilities. Desalination 2021;504:114952.

[62] Alba SO, Manana M, Ortega Alba S, Manana M. Characterization and analysis of energy demand patterns in airports. Energies 2017;10:119. 2017–01–19;10.

[63] Kakoulaki G, Kougias I, Taylor N, Dolci F, Moya J, Jäger-Waldau A. Green hydrogen in Europe – a regional assessment: substituting existing production with electrolysis powered by renewables. Energy Convers Manag 2021/01/15:228.

[64] Sobu A, Wu G. Optimal operation planning method for isolated micro grid considering uncertainties of renewable power generations and load demand. 2012.

[65] Wolleswinkel RE, de Vries R, Hoogreef MFM, Vos R. A new perspective on battery-electric aviation, part I: reassessment of achievable range. 2024.